NASA Contractor Report 178293

Development of Response Models for the Earth Radiation Budget Experiment (ERBE) Sensors:

Part II – Analysis of the ERBE Integrating Sphere Ground Calibration

Nesim Halyo and Deborah B. Taylor

Information & Control Systems, Incorporated
Hampton, Virginia 23666

Contract NAS1-16130

March 20, 1987

National Aeronautics and
Space Administration

Langley Research Center
Hampton, Virginia 23665-5225

FOREWORD

This report entitled "Development of Response Models for the Earth Radiation Budget Experiment (ERBE) Sensors" consists of the following four parts.

Part I, NASA CR-178292, is entitled "Dynamic Models and Computer Simulations for the ERBE Nonscanner, Scanner and Solar Monitor Sensors".

This is Part II, NASA CR-178293, entitled "Analysis of the ERBE Integrating Sphere Ground Calibration".

Part III, NASA CR-178294, is entitled "ERBE Scanner Measurement Accuracy Analysis Due to Reduced Housekeeping Data".

Part IV, NASA CR-178295, is entitled "Preliminary Nonscanner Models and Count Conversion Algorithms".

Abstract

A two-part study of the buckling and postbuckling behavior of laminated anisotropic plates with bending-extensional coupling is presented. The first part involves the development and application of a modified Rayleigh-Ritz analysis technique. Modifications made to the classical technique can be grouped into three areas. First, known symmetries of anisotropic panels are exploited in the selection of approximation functions. Secondly, a reduced basis technique based on these same symmetries is applied in the linear range. Finally, geometric boundary conditions are enforced via an exterior penalty function approach, rather than relying on choice of approximation functions to satisfy these boundary conditions. Numerical results are presented for both the linear and nonlinear range, with additional studies made to determine the effect of variation in penalty parameter and number of basis vectors.

In the second portion of the study, six panels possessing anisotropy and bending-extensional coupling are tested and detailed comparisons are made between experiment and finite element results in order to gain insight into the postbuckling and failure characteristics of such panels. The panels are constructed using two different lamination sequences, and panels with three different aspect ratios were constructed for each lamination sequence.

ABSTRACT

An explicit solution of the spectral radiance leaving an arbitrary point on the wall of a spherical cavity with diffuse reflectivity is obtained. The solution is applicable to spheres with an arbitrary number of openings of any size and shape, an arbitrary number of light sources with possibly non-diffuse characteristics, a non-uniform sphere wall temperature distribution, non-uniform and non-diffuse sphere wall emissivity and non-uniform but diffuse sphere wall spectral reflectivity. A general measurement equation describing the output of a sensor with a given field of view, angular and spectral response measuring the sphere output is obtained. The results are applied to the Earth Radiation Budget Experiment (ERBE) integrating sphere. The sphere wall radiance uniformity, loading effects and non-uniform wall temperature effects are investigated. It is shown that using appropriate interpretation and processing, a high-accuracy shortwave calibration of the ERBE sensors can be achieved.

TABLE OF CONTENTS

LIST OF FIGURES

LIST OF TABLES

I. INTRODUCTION

Due to their versatility, integrating spheres have found a large variety of uses ranging from the measurement of spectral reflectance to more recent laser power measurement applications [1] - [11]. In the Earth Radiation Budget Experiment (ERBE), the integrating sphere was used to provide a precision calibration source which resembles Earth radiation in spectral content and width of field-of-view for the seven Earth-viewing ERBE sensors [12] - [17]. In this application, the integrating sphere is used to generate both shortwave and longwave radiation. Since both narrow field-of-view (scanner) and wide field-of-view (non-scanner) sensors were calibrated using the ERBE integrating sphere, the spectral radiance leaving the sphere wall must be accurately known.

The theory of integrating spheres has been reported in References [18] - [25]. Most of these papers consider special cases. The most general result obtained is that for a sphere with diffuse reflectance, the reflected radiant incidence satisfies a Fredholm equation of the 2^{nd} kind [18], [19]. In [19], this integral equation is solved by applying the method of resolvents for geometries usually encountered in measuring sample reflectivities. To reduce the computational burden of the resolvent approach, [24], [25] use the net radiation method to obtain the solution for similar cases. In [21] and [22], a sphere with a single spherical port of arbitrary size, uniform diffuse wall reflectance and absorptance is considered with surface properties independent of wavelength. The absorption and emission characteristics of such a sphere with uniform wall temperature are investigated in [21] for diffuse and non-diffuse source illumination. In [22], an analytical solution to the governing integral equation is obtained for the above sphere with non-uniform wall temperature distribution, but with diffuse source illumination through the spherical port. While a variety of individual cases have been solved, a general solution describing the spectral radiance at an arbitrary point

on the sphere wall for use in analyzing complex cases such as the ERBE integrating sphere is not available.

In this paper, an explicit solution of the spectral radiance leaving an arbitrary point on the wall of an integrating sphere is obtained by solving a Fredholm equation of the 2^{nd} kind (describing the flux) analytically. The solution is applicable to spherical cavities with an arbitrary number of non-uniform light sources with non-diffuse directional characteristics, an arbitrary number of spherical ports of any size and shape, non-uniform but diffuse sphere wall spectral reflectivity, non-uniform and non-diffuse wall emissivity, and non-uniform sphere wall temperature distribution. The generality of the solution for the spectral radiance and the radiant incidence can be used to analyze the errors and uncertainties introduced by situations where the usual assumptions are only partially valid.

A general measurement equation is obtained to describe and analyze the output of a sensor with a given spectral and angular response. The sensor is assumed to be placed at one of the exit ports, and may have a point-spread function corresponding to a narrow or wide field-of-view sensor. A number of special cases are considered to see the effects of a small detector surface, diffuse emissivity and piece-wise constant sphere surface properties on the measurement equation and the sphere output.

In Section III, the general expression for the spectral radiance and the measurement equation are applied to the ERBE integrating sphere. The uniformity of the sphere wall radiation when viewed by a narrow field-of-view scanner, the loading effects or increased sphere output due to the presence of the measuring sensor and other unexpected behavior is analyzed. Finally, an approach for calibrating the sphere photo-diodes to provide an accurate calibration source for the ERBE Shortwave sensors is presented.

II. THEORETICAL CONSIDERATIONS

Explicit Solution of the Spectral Radiance.

Consider a sphere, shown in Figure 1, whose inner surface is illuminated by an arbitrary light source with spectral radiance $L_{so\lambda}(\theta,\phi;\psi,\chi)$ leaving the surface at the point (θ,ϕ) in the direction (ψ,χ). In general, the source radiance can be distributed over the sphere surface or simply be a point source, and may be non-diffuse. The sphere surface may have any number of openings or ports.

To understand the significance of the usual assumptions made, such as uniform source illumination, uniform sphere wall temperature, uniform diffuse emissivity, etc., we will first attempt to obtain a solution with the least number of assumptions, and then consider individual situations as special cases of the more general solution. This approach allows the analysis of situations where the assumptions are only partially valid, using sensitivity analysis.

Thus, let $T(\theta,\phi)$ be the temperature at the point (θ,ϕ), $\epsilon_\lambda(\theta,\phi;\psi,\chi;T)$ the directional spectral emissivity at the point (θ,ϕ) and temperature T , $\rho'_\lambda(\theta,\phi;\psi_i,\chi_i;\psi_r,\chi_r)$ the directional spectral reflectivity at the point (θ,ϕ) for radiation arriving from the direction (ψ_i,χ_i) and reflected in the direction (ψ_r,χ_r). Let $L_{i\lambda}(\theta,\phi;\psi,\chi)$ represent the spectral radiance incident at the point (θ,ϕ) from the direction (ψ,χ), and $L_{o\lambda}(\theta,\phi;\psi,\chi)$ the spectral radiance leaving the point (θ,ϕ) in the direction (ψ,χ). Finally, if radiation leaves the point (θ,ϕ) in the direction (ψ,χ), the point and direction of incidence will be denoted by (θ',ϕ') and (ψ',χ'), respectively.

In this notation, the general radiative equations can be expressed as

$$L_{o\lambda}(\theta,\phi;\psi,\chi) = L_{so\lambda}(\theta,\phi;\psi,\chi) + \epsilon_\lambda(\theta,\phi;\psi,\chi;T(\theta,\phi))\frac{c_1\lambda^{-5}}{e^{c_2/\lambda T(\theta,\phi)}-1} + \iint_{\Omega_o} L_{i\lambda}(\theta,\phi;\psi_i,\chi_i)\rho'_\lambda(\theta,\phi;\psi_i,\chi_i;\psi,\chi)d\Omega(\psi,\chi) \quad (1)$$

$$L_{i\lambda}(\theta,\phi;\psi,\chi) = L_{o\lambda}(\theta',\phi';\psi',\chi') \quad , \quad (2)$$

$$d\Omega(\psi,\chi) = \cos\chi \sin\chi \, d\chi \, d\psi \quad , \quad (3)$$

where $L_{so\lambda}(\theta,\phi;\psi,\chi)$ is the spectral radiance of a source, leaving the point (θ,ϕ) in the direction (ψ,χ), and Ω_o denotes a hemisphere. For simplicity, let $T' = T(\theta',\phi')$, and

$$L_B(\lambda,T) = \frac{c_1\lambda^{-5}}{e^{c_2/\lambda T}-1} \quad (4)$$

Combining (1) and (2) results in the integral equation

$$L_{i\lambda}(\theta,\phi;\psi,\chi) = L_{so\lambda}(\theta',\phi';\psi',\chi') + \epsilon_\lambda(\theta',\phi';\psi',\chi';T')L_B(\lambda,T') + \iint_{\Omega_o} L_{i\lambda}(\theta',\phi';\psi_i,\chi_i)\rho'_\lambda(\theta',\phi';\psi_i,\chi_i;\psi',\chi')d\Omega(\psi_i,\chi_i) \quad (5)$$

The integral equation (5) represents the most general case for an arbitrary cavity. In the following, we will obtain a solution to (5) for a spherical cavity, assuming that the surface spectral reflectivity is diffuse, but not necessarily uniform; i.e.,

$$\rho'_\lambda(\theta,\phi;\psi_i,\chi_i;\psi_r,\chi_r) = \frac{1}{\pi}\rho_\lambda(\theta,\phi) \quad . \quad (6)$$

where $\rho_\lambda(\theta,\phi)$ is the spectral reflectivity at the point (θ,ϕ).

Then a general solution to (5) becomes possible for the case of a sphere. In this case, the reflected spectral radiance can be expressed as

$$L_{r\lambda}(\theta,\phi;\psi_r,\chi_r) = \frac{1}{\pi}\iint_{\Omega_o} L_{i\lambda}(\theta,\phi;\psi_i,\chi_i)\rho_\lambda(\theta,\phi)d\Omega(\psi_i,\chi_i) \tag{7}$$

$$= \frac{1}{\pi}\rho_\lambda(\theta,\phi)E_\lambda(\theta,\phi) \quad , \tag{8}$$

where $E_\lambda(\theta,\phi)$ is the spectral radiant incidence at the point (θ,ϕ). Substituting (8) into (5),

$$\begin{aligned} L_{i\lambda}(\theta,\phi;\psi,\chi) = {} & L_{oo\lambda}(\theta',\phi';\psi',\chi') \\ & + \epsilon_\lambda(\theta',\phi';\psi',\chi';T')L_B(\lambda,T') \\ & + \frac{1}{\pi}\rho_\lambda(\theta',\phi')E_\lambda(\theta',\phi') \quad . \end{aligned} \tag{9}$$

Now recall that for a spherical surface

$$\iint_{\Omega_o} L_{i\lambda}(\theta,\phi;\psi,\chi)d\Omega(\psi,\chi) = \frac{1}{4R^2}\iint_{A_o} L_{i\lambda}(\theta,\phi;\psi,\chi)dA(\theta',\phi') \tag{10}$$

Integrating (9),

$$\begin{aligned} E_\lambda(\theta,\phi) &= \iint_{\Omega_o} L_{i\lambda}(\theta,\phi;\psi,\chi)d\Omega(\psi,\chi) \\ &= \frac{1}{4R^2}\iint_{A_o} L_{i\lambda}(\theta,\phi;\psi,\chi)dA(\theta',\phi') \end{aligned} \tag{11}$$

$$= \iint_{\Omega_o} L_{so\lambda}(\theta', \phi'; \psi', \chi') d\Omega(\psi, \chi)$$
$$+ \frac{1}{4R^2} \iint_{A_s} \epsilon_\lambda(\theta', \phi'; \psi', \chi'; T') L_B(\lambda, T') dA(\theta', \phi')$$
$$+ \frac{1}{4\pi R^2} \iint_{A_s} \rho_\lambda(\theta', \phi') E_\lambda(\theta', \phi') dA(\theta', \phi') \quad . \tag{12}$$

Let $E_{s\lambda}(\theta, \phi)$ denote the radiant incidence at (θ, ϕ) produced by the light sources directly; i.e., without considering any reflections; then,

$$E_{s\lambda}(\theta, \phi) = \iint_{\Omega_o} L_{so\lambda}(\theta', \phi'; \psi', \chi') d\Omega(\psi, \chi) \tag{13}$$

Similarly, let $E_{e\lambda}(\theta, \phi)$ denote the radiant incidence at the point (θ, ϕ) due to emitted energy before reflections are considered; then,

$$E_{e\lambda}(\theta, \phi) = \iint_{\Omega_o} \epsilon_\lambda(\theta', \phi'; \psi', \chi', T') L_B(\lambda, T') d\Omega(\psi, \chi)$$
$$= \frac{1}{4R^2} \iint_{A_s} \epsilon_\lambda(\theta', \phi'; \psi', \chi', T') L_B(\lambda, T') dA(\theta', \phi') \tag{14}$$

Both of the terms $E_{s\lambda}(\theta, \phi)$ and $E_{e\lambda}(\theta, \phi)$ are known when the location and directional characteristics of the light sources, the emissivity and temperature distribution are known. The integral equation (12) can now be expressed as

$$E_\lambda(\theta, \phi) = E_{s\lambda}(\theta, \phi) + E_{e\lambda}(\theta, \phi)$$
$$+ \frac{1}{4\pi R^2} \iint_{A_s} \rho_\lambda(\theta', \phi') E_\lambda(\theta', \phi') dA(\theta', \phi') \quad . \tag{15}$$

Note that the integration in (15) is done over the total spherical surface A_s, so that the last term in (15) is independent of the spatial variables (θ, ϕ). It follows that the spectral radiant incidence has the form

$$E_\lambda(\theta,\phi) = E_{s\lambda}(\theta,\phi) + E_{e\lambda}(\theta,\phi) + C_\lambda \tag{16}$$

where C_λ may vary with wavelength, but is spatially uniform,

$$C_\lambda = \frac{1}{4\pi R^2} \iint_{A_s} \rho_\lambda(\theta',\phi') E_\lambda(\theta',\phi') dA(\theta',\phi') \tag{17}$$

To obtain C_λ, it suffices to substitute (16) into (15), and solve for C_λ.

$$C_\lambda = \frac{1}{1-\bar{\rho}_\lambda} \frac{1}{4\pi R^2} \iint_{A_s} \rho_\lambda(\theta',\phi') \Big[E_{s\lambda}(\theta',\phi') + E_{e\lambda}(\theta',\phi') \Big] dA(\theta',\phi') \quad , \tag{18}$$

$$\bar{\rho}_\lambda = \frac{1}{4\pi R^2} \iint_{A_s} \rho_\lambda(\theta',\phi') dA(\theta',\phi') \quad , \tag{19}$$

$$\begin{aligned} E_\lambda(\theta,\phi) = {} & E_{s\lambda}(\theta,\phi) + \frac{1}{1-\bar{\rho}_\lambda} \frac{1}{4\pi R^2} \iint_{A_s} \rho_\lambda(\theta',\phi') E_{s\lambda}(\theta',\phi') dA(\theta',\phi') \\ & + E_{e\lambda}(\theta,\phi) + \frac{1}{1-\bar{\rho}_\lambda} \frac{1}{4\pi R^2} \iint_{A_s} \rho_\lambda(\theta',\phi') E_{e\lambda}(\theta',\phi') dA(\theta',\phi') \ . \end{aligned} \tag{20}$$

The expression in (20) is the general solution of the spectral radiant incidence for a spherical cavity with diffuse reflectivity, where the effects of the source radiance and emitted energy are shown explicitly. Similarly, the spectral radiance leaving any point (θ,ϕ) in an arbitrary direction (ψ,χ) can be obtained by substituting (8) and (20) into (1)

$$\begin{aligned} L_{o\lambda}(\theta,\phi;\psi,\chi) = {} & L_{so\lambda}(\theta,\phi;\psi,\chi) + \frac{1}{\pi}\rho_\lambda(\theta,\phi) E_{s\lambda}(\theta,\phi) \\ & + \frac{\rho_\lambda(\theta,\phi)}{\pi(1-\bar{\rho}_\lambda)} \frac{1}{4\pi R^2} \iint_{A_s} \rho_\lambda(\theta',\phi') E_{s\lambda}(\theta',\phi') dA(\theta',\phi') \\ & + \epsilon_\lambda(\theta,\phi;\psi,\chi;T(\theta,\phi)) L_B(\lambda,T(\theta,\phi)) + \frac{1}{\pi}\rho_\lambda(\theta,\phi) E_{e\lambda}(\theta,\phi) \\ & + \frac{\rho_\lambda(\theta,\phi)}{\pi(1-\bar{\rho}_\lambda)} \frac{1}{4\pi R^2} \iint_{A_s} \rho_\lambda(\theta',\phi') E_{e\lambda}(\theta',\phi') dA(\theta',\phi') \end{aligned} \tag{21}$$

The general solution for the spherical cavity with diffuse reflectivity is thus given by (19) - (21), (13) and (14). It should be noted that the solution shows the effects of multiple sources with non-diffuse characteristics, diffuse but non-uniform spectral reflectivity, non-uniform wall temperatures, and non-uniform and non-diffuse spectral emissivity.

The ability to account for multiple non-diffuse sources provides a tool to analyze the, sometimes non-negligible, effects of "loading" (radiation reflected and emitted) by the instrument measuring the flux or radiance at the exit port, or analyze the effects of stray radiation entering the sphere through the exit port(s). The loading effects observed in the calibration of the Earth Radiation Budget Experiment (ERBE) instruments will be analyzed in the following sections. Non-uniform reflectivity and emissivity allows the analysis of multiple ports of any size and of material properties of surfaces such as filters, diffuser plates, samples, etc. Non-uniform temperature distribution allows the analysis of port surfaces such as filters or diffuser plates which may be at substantially different temperatures than the wall temperature, particularly when the instrument at the exit port measures some emitted energy.

It is of interest to note that, for the relatively general case considered in (20), the incident flux on the sphere varies only according to the source irradiation $E_{s\lambda}(\theta, \phi)$ and the non-diffuse emission $E_{e\lambda}(\theta, \phi)$. Thus, for a spherical exit port which is not irradiated by the source, and diffusely emitting surface, the flux at every point of the exit port will be constant, despite the possible variations of the spectral reflectivity and emissivity on the sphere wall and other ports, and non-uniformities in the wall and port temperatures. Furthermore, the percentage variation is likely to be small when the average sphere reflectivity is close to unity, while the emissivity at the corresponding wavelength is small. Also note that, for the diffuse emission case, the spectral radiance leaving points which do not contain a light source is diffuse, but its magnitude varies over the sphere surface. Due to the variation in magnitude, the radiance incident on the exit port will not have a diffuse character except for special cases.

It should be noted that the cases of a single port of arbitrary size with uniform reflectivity and emissivity considered in [21], [22], as well as other previous results, can be easily obtained from the general solution as special cases. Also note that the emitted energy, $E_{e\lambda}(\theta,\phi)$, can be considered to be another source of radiation in $E_{s\lambda}(\theta,\phi)$, as evidenced by (20) and (21).

It is sometimes of interest to obtain the flux at the exit port or at other points on the sphere. This can be easily achieved using the spectral radiant incidence expression in (20).

$$E(\theta,\phi) = \int_o^\infty E_\lambda(\theta,\phi)d\lambda = E_s(\theta,\phi) + E_e(\theta,\phi) + \frac{1}{4\pi R^2}\iint_{A_s}\left(\int_o^\infty \frac{\rho_\lambda(\theta',\phi')}{1-\bar{\rho}_\lambda}\Big[E_{s\lambda}(\theta',\phi') + E_{e\lambda}(\theta',\phi')\Big]d\lambda\right)dA(\theta',\phi') \quad (22)$$

When the spectral reflectivity, $\rho_\lambda(\theta,\phi)$, is independent of wavelength, the emissivity and reflectivity are uniform and diffuse on the sphere wall, A_w, and the exit ports have zero reflectivity and emissivity, the radiant incidence simplifies to the well-known expression [21], [22]

$$E(\theta,\phi) = E_s(\theta,\phi) + \frac{1/A_s}{1-\bar{\rho}}\left[\rho_w P_w + \iint_{A_w}\epsilon_w(T)\sigma\, T^4(\theta,\phi)\, dA(\theta,\phi)\right] \quad , \quad (23)$$

$$P_w = \iint_{A_w} E_s(\theta,\phi)dA(\theta,\phi) \quad , \quad \bar{\rho} = \rho_w\frac{A_w}{A_s} \quad , \quad A_s = 4\pi R^2 \quad , \quad (24)$$

where ρ_w and ϵ_w are the sphere wall reflectance and emittance, respectively, and P_w is the source power irradiating the sphere wall. Note that the input source is arbitrary, and need not be diffuse or uniform, while multiple ports may be present. If the incoming source is diffuse, (23) further simplifies to [22]

$$E(\theta,\phi) = \frac{1/A_s}{1-\bar{\rho}}\left[P + \iint_{A_w}\epsilon_w(T)\sigma\, T^4(\theta,\phi)\, dA(\theta,\phi)\right] \quad (25)$$

$$P = \iint_{A_s} E_s(\theta,\phi)\, dA(\theta,\phi) = \iint_{A_s} \iint_{\Omega_o} L_{so}(\theta,\phi;\psi,\chi)\, d\Omega(\psi,\chi)\, dA(\theta,\phi) \qquad (26)$$

where P is the total source power entering the sphere.

It is important to note that in the most common case where the spectral reflectivity, $\rho_\lambda(\theta,\phi)$, depends on wavelength in a non-trivial manner, (23) and (25) are not valid, and the more general form given in (22) must be used. In this case, the input source and emitted radiation spectra are modified by the spectral reflectivity characteristics of the sphere wall; so that the spectrum of the radiation changes with every reflection from the sphere wall. Thus, the irradiance leaving the sphere may, in some cases, have a significantly different spectrum than the incoming radiation.

Whereas the irradiance at the exit port can be obtained using the appropriate expression, the measurement obtained from a sensor placed at the exit port can be different than this irradiance. This is largely due to the fact that most sensors have a field-of-view somewhat smaller than a hemisphere, with less than perfect angular response and spectral characteristics. These effects can be analyzed using the analtyical solution of the spectral radiance given by (21) for radiation leaving an arbitrary point in an arbitrary direction.

The General Measurement Equation.

Consider a sensor measuring the radiation incident on its detector surface. Let $\tau_{d\lambda}(\psi',\chi')$ be the spectral and angular response of the sensor, and $L_{d\lambda}(x,y;\psi',\chi')$ the spectral radiance incident at the point (x,y) from the direction (ψ',χ'). Then the sensor output can be expressed in the form:

$$m = K \int_o^\infty \iint_{A_d} \iint_{\Omega(x,y)} L_{d\lambda}(x,y;\psi',\chi')\tau_{d\lambda}(\psi',\chi')d\Omega(\psi',\chi')dA(x,y)d\lambda + n \quad , \qquad (27)$$

where $\Omega(x,y)$ corresponds to the solid angle at the point (x,y) which "sees" the integrating sphere surface, and n represents the sensor noise and errors in accounting for radiation

from outside the field of view of interest. Since $L_{d\lambda}(x,y;\psi',\chi')$ is the spectral radiance leaving the sphere from (θ,ϕ) along (ψ,χ) and arrives at the point (x,y) on the detector,

$$m = K\int_o^\infty \iint_{A_d} \iint_{A_s(x,y)} L_{o\lambda}(\theta,\phi;\psi,\chi)\tau_{d\lambda}(\psi',\chi') \frac{\cos\chi\cos\chi'}{r^2} dA_s(\theta,\phi)dA(x,y)d\lambda + n \tag{28}$$

where $A_s(x,y)$ is the footprint or the surface on the sphere that "sees" the point (x,y), r is the distance between (x,y) and (θ,ϕ), and $L_{o\lambda}(\theta,\phi;\psi,\chi)$ is given by (21).

In the following, assume that the light sources do not directly irradiate the detector surface A_d, which is the usual configuration; i.e., $L_{so\lambda}(\theta,\phi;\psi,\chi) = 0$, when (θ,ϕ) is in $A_s(x,y)$. Further assume that the detector's spectral and angular responses are independent of each other; i.e.,

$$\tau_{d\lambda}(\psi',\chi') = \tau(\lambda)\tau_d(\psi',\chi') \quad . \tag{29}$$

Small Detector Surface.

If the area of the detector is small enough that $\epsilon_\lambda(\theta,\phi;\psi,\chi;T)$ is almost constant while (ψ,χ) scans the detector surface, then the measurement equation simplifies to

$$m = K\iint_{A_s} S(\theta,\phi)\left[\int_o^\infty \tau(\lambda)L_{o\lambda}(\theta,\phi;\psi,\chi)d\lambda\right]dA(\theta,\phi) + n \quad , \tag{30}$$

$$S(\theta,\phi) = \iint_{A_d} I(x,y;\theta,\phi)\tau_d(\psi',\chi')\frac{\cos\chi\cos\chi'}{r^2}dA_d(x,y) \quad , \tag{31}$$

where $I(x,y;\theta,\phi)$ is unity when (x,y) and (θ,ϕ) can see each other, and vanishes otherwise. Note that the point spread function $S(\theta,\phi)$ vanishes for points (θ,ϕ) that do not see any part of the detector surface (ψ,χ) is taken to be the direction from (θ,ϕ) to the center of the detector surface.

Diffuse Emittance.

Several simplifications can be made in the general solution when the spectral directional emissivity is diffuse, i.e.,

$$\epsilon_\lambda(\theta,\phi;\psi,\chi;T) = \frac{1}{\pi}\epsilon_\lambda(\theta,\phi;T) \quad . \tag{32}$$

By observation of (14)

$$E_{e\lambda}(\theta,\phi) = \frac{1}{4\pi R^2}\iint_{A_s} \epsilon_\lambda(\theta',\phi';T(\theta',\phi'))L_B(\lambda,T(\theta',\phi')dA(\theta',\phi')) \quad . \tag{33}$$

Irrespective of the size of the ports and non-uniform temperature distribution, $E_{e\lambda}(\theta,\phi)$ is constant at any point on the sphere. The spectral irradiance in (20) simplifies to

$$E_\lambda(\theta,\phi) = E_{s\lambda}(\theta,\phi) + \frac{1}{1-\bar{\rho}_\lambda}\frac{1}{4\pi R^2}\iint_{A_s} \rho_\lambda(\theta',\phi')E_{s\lambda}(\theta',\phi')dA(\theta',\phi') + \frac{E_{e\lambda}}{1-\bar{\rho}_\lambda} \tag{34}$$

Similarly,

$$\begin{aligned} L_{o\lambda}(\theta,\phi;\psi,\chi) = {} & L_{so\lambda}(\theta,\phi;\psi,\chi) + \frac{1}{\pi}\rho_\lambda(\theta,\phi)E_{s\lambda}(\theta,\phi) \\ & + \frac{\rho_\lambda(\theta,\phi)}{\pi(1-\bar{\rho}_\lambda)}\frac{1}{4\pi R^2}\iint_{A_s} \rho_\lambda(\theta',\phi')E_{s\lambda}(\theta',\phi')dA(\theta',\phi') \\ & + \frac{1}{\pi}\epsilon_\lambda(\theta,\phi;T(\theta,\phi))L_B(\lambda,T(\theta,\phi)) + \frac{\rho_\lambda(\theta,\phi)}{\pi(1-\bar{\rho}_\lambda)}E_{e\lambda} \end{aligned} \tag{35}$$

The measurement in (28) simplifies to

$$m = K\iint_{A_s} S(\theta,\phi)\left[\int_o^\infty \tau(\lambda)L_{o\lambda}(\theta,\phi)d\lambda\right]dA_s + n \quad , \tag{36}$$

irrespective of the detector size.

Piece-wise Constant Surface Properties.

In most applications of the integrating sphere, the sphere surface consists of the sphere wall and a number of ports such as the sample, standard, entrance or exit ports. Over each port (sometimes portions of a port) and the wall surface, the spectral reflectivity and emissivity, and temperature are assumed to be constant. The effects of small variations due to non-perfect surface properties can be analyzed using the more general case given in (34) - (36).

Thus, suppose that the sphere is divided into N areas $\{A_k,\ k = 1, 2, ..., N\}$ of arbitrary size and shape over which

$$\rho_\lambda(\theta,\phi) = \rho_{\lambda k}\ ,\ \epsilon_\lambda(\theta,\phi;T(\theta,\phi)) = \epsilon_{\lambda k}\ ,\ T(\theta,\phi) = T_k\ ,\ (\theta,\phi)\epsilon A_k \tag{37}$$

Note that the temperature can vary from on subsurface to another, and the source irradiation remains arbitrary. Then

$$E_{e\lambda} = \sum_{k=1}^{N} f_k \epsilon_{\lambda k} L_B(\lambda, T_k) \quad , \tag{38}$$

$$f_k = \frac{|A_k|}{4\pi R^2} = \frac{|A_k|}{|A_s|} \quad , \tag{39}$$

$$\bar{\rho}_\lambda = \sum_{k=1}^{N} f_k \rho_{\lambda k} \quad , \tag{40}$$

$$E_\lambda(\theta,\phi) = E_{s\lambda}(\theta,\phi) + \frac{1}{1-\bar{\rho}_\lambda} \sum_{k=1}^{N} f_k \rho_{\lambda k} \bar{E}_{s\lambda k} + \frac{E_e\lambda}{1-\bar{\rho}_\lambda} \quad , \tag{41}$$

$$\bar{E}_{s\lambda k} = \frac{1}{|A_k|} \iint_{A_k} E_{s\lambda}(\theta',\phi') dA(\theta',\phi') \quad , \tag{42}$$

$$L_{o\lambda}(\theta,\phi;\psi,\chi) = L_{so\lambda}(\theta,\phi;\psi,\chi) + \frac{1}{\pi}\rho_{\lambda k}E_{s\lambda}(\theta,\phi)$$
$$+ \frac{\rho_{\lambda k}}{\pi(1-\bar{\rho}_\lambda)}\sum_{j=1}^{N} f_j\rho_{\lambda j}\bar{E}_{s\lambda j} + \frac{1}{\pi}\epsilon_{\lambda k}L_B(\lambda,T_k)$$
$$+ \frac{\rho_{\lambda k}}{\pi(1-\bar{\rho}_\lambda)}E_{e\lambda} \quad , \quad (\theta,\phi)\epsilon A_k \quad , \tag{43}$$

$$m = \frac{K}{\pi}\int_o^\infty \tau(\lambda)\Bigg[\sum_{k=1}^{N}\rho_{\lambda k}\Bigg(\iint_{A_k} S(\theta,\phi)E_{s\lambda}(\theta,\phi)dA(\theta,\phi)\Bigg)$$
$$+ \left(\sum_{k=1}^{N}\frac{S_k\rho_{\lambda k}}{1-\bar{\rho}_\lambda}\right)\left(\sum_{k=1}^{N} f_k\rho_{\lambda k}\bar{E}_{s\lambda k}\right) + \left(\sum_{k=1}^{N} S_k\epsilon_{\lambda k}L_B(\lambda,T_k)\right)$$
$$+ \left(\sum_{k=1}^{N}\frac{S_k\rho_{\lambda k}}{1-\bar{\rho}_\lambda}\right)\left(\sum_{k=1}^{N} f_k\epsilon_{\lambda k}L_B(\lambda,T_k)\right)\Bigg]d\lambda + n \quad , \tag{44}$$

$$S_k = \iint_{A_k} S(\theta,\phi)dA(\theta,\phi)$$
$$= \iint_{A_k}\iint_{A_d} I(x,y;\theta,\phi)\tau_d(\psi',\chi')\frac{\cos\chi\cos\chi'}{r^2}dA_d(x,y)dA(\theta,\phi) \quad . \tag{45}$$

III. ANALYSIS OF THE ERBE INTEGRATING SPHERE

The Earth Radiation Budget Experiment (ERBE) integrating sphere was designed for use in the ground calibration of the ERBE instruments consisting of four non-scanners, three scanners and a solar monitor. The primary calibration source for the Earth-viewing instruments is the Master Reference Black Body (MRBB). The ERBE integrating sphere provides a calibration source which more closely approximates the Earth's spectral mix of short and longwave radiation by providing emitted radiation from the sphere wall and shortwave reflected radiation originating from four Tungsten lamps.

The ERBE integrating surface can be divided into five surfaces

A_1 - the sphere wall

A_2 - four entrance ports

A_3 - two Silicon Photo-diode (SiPd) ports

A_4 - exit port edge

A_5 - exit port

The entrance ports are covered by flashed opal glass held in place by an insulator to provide a diffuse source radiation for uniformity. The sphere wall uses $KodakBaSO_4$ paint for reflectance properties. The exit port is used to view the inner surface of the sphere with each of the seven Earth-viewing ERBE instruments. The instrument's detecting surfaces do not directly view the Tungsten lamp sources. Similarly, the photo-diode field-of-view does not include the entrance port.

During the ground calibration the integrating sphere data showed the following characteristics:

1) The Narrow field-of-view scanning sensors measure non-uniformities (8 %) on the sphere wall after known sources of error are taken into account to the extent possible.

2) The Medium Field-of-View (MFOV) non-scanner consistently measures a higher irradiance than the Wide Field-of-View (WFOV) non-scanner sensor for both longwave and shortwave radiation.

3) The integrating sphere photo-diode response shows nonlinear characteristics relative to the non-scanner measurements.

4) With the lamps off, the non-scanner sensors measure a higher (longwave) irradiance than expected by about 10 - 20 W/m^2.

The following analysis of the ERBE integrating sphere ground calibration attempts to determine possible causes of the unexpected characteristics mentioned above. Assuming the physical causes considered here are mainly responsible for these characteristics results in a linear response for the photo-diode, and a shortwave calibration of high accuracy for the WFOV and MFOV Total Waveband channels using the integrating sphere. The error standard deviation thus obtained is $.73W/m^2$ for the WFOV instrument, and $1.52W/m^2$ for MFOV instrument. It is interesting to note that since the shortwave measurements are obtained by the difference of two measurements, the errors corresponding to a single measurement are $.51W/m^2$ for the WFOV, and $1.07W/m^2$ for the MFOV instruments.

From (35), a measurement made by the ERBE instruments or the SiPd's can be expressed as:

$$m = \frac{K}{\pi}\int_o^\infty \tau(\lambda)\Bigg[\rho_{\lambda 1}\Big(\iint_{A_1} S(\theta,\phi)E_{o\lambda}(\theta,\phi)dA\Big) + \left(\frac{S_1\rho_{\lambda 1}}{1-\bar{\rho}_\lambda}\right)\Big(\sum_{k=1}^{N} f_k\rho_{\lambda k}\bar{E}_{o\lambda k}\Big) + S_1\epsilon_{\lambda 1}L_B(\lambda,T_1) + \left(\frac{S_1\rho_{\lambda 1}}{1-\bar{\rho}_\lambda}\right)\Big(\sum_{k=1}^{N} f_k\epsilon_{\lambda k}L_B(\lambda,T_k)\Big)\Bigg]\,d\lambda + n \qquad (46)$$

$$S_k = 0 \quad , \quad k = 2,3,4,5 = N \quad . \qquad (47)$$

Wall Uniformity.

For purposes of calibration of the ERBE instruments, it is desirable to have the portion of the integrating sphere wall viewed by any of the sensors to be uniform. Then each sensor would view the same radiance irrespective of its field of view. From (46) or (43), uniformity requires that the total direct source irradiation on the sphere wall, including any loading effects, be constant, assuming that the reflectivity, emissivity and temperature are uniform. Thus, it is necessary for the light sources to be diffuse. The opal diffuser plates serve this purpose.

Consider the non-uniformity effects that may be produced by a non-diffuse light source. This case would represent an opal glass diffuser which is not perfectly uniform in all directions. Let the source spectral radiance at one of the entrance ports be $1/\pi\, E_{so\lambda} f(\chi)$. Then from (13):

$$E_{s\lambda}(\theta,\phi) = \frac{1}{4\pi R^2} \iint_A E_{so\lambda} f(\chi') dA(\theta',\phi') \quad , \tag{48}$$

where A is the surface of one entrance port. Since χ' is nearly constant over A,

$$E_{s\lambda}(\theta,\phi) \simeq \frac{E_{so\lambda}|A|}{4\pi R^2} f(\chi') = \frac{P_{s\lambda}}{|A_s|} f(\chi) \quad , \tag{49}$$

$$\chi_i = cos^{-1}\left(\frac{r_i(\theta,\phi)}{2R}\right) \quad , \quad i = 1,2,3,4 \tag{50}$$

where $r_i(\theta,\phi)$ is the distance between the point (θ,ϕ) and the location of the i^{th} entrance port. The total irradiation from the four Tungsten lamps is

$$E_{s\lambda}(\theta,\phi) = \sum_{i=1}^{4} \frac{P_{s_i\lambda}}{|A_s|} f\left(cos^{-1}\frac{r_i(\theta,\phi)}{2R}\right) \quad . \tag{51}$$

From (43), it is seen that the variation in the wall spectral radiance will be due to the term containing $E_{s\lambda}(\theta,\phi)$, as the other terms remain constant. Figure 2(a) shows the normalized shortwave wall radiance resulting from four lamps of equal power, when 82 %

of the lamp power is distributed in a perfectly diffuse manner, while 18 % is concentrated in the range $0 \leq \chi \leq \chi_c$, $(\chi_c = 9^o)$ according to $\left[1 + \left(\chi/\chi_c\right)^8\right]^{-1}$.

On the other hand, if a narrow field-of-view (NFOV) shortwave sensor scans the wall surface from 5 inches outside the sphere exit port, then its measurement will be

$$\frac{K}{\pi} \iint_{A_s} S(\theta,\phi) \int_o^\infty \tau(\lambda)\rho_{\lambda 1}\left[E_{s\lambda}(\theta,\phi) + \frac{\rho_{\lambda 1}\bar{E}_{s\lambda 1}}{1-\bar{\rho}_\lambda}\right] d\lambda\, dA(\theta,\phi) + n \quad . \tag{52}$$

After substitution of (31) into (52), and some manipulation with small angle approximations, (52) can be approximated by

$$m_\beta = \frac{K\,|A_d|\,|\omega_{FOV}|}{\pi|A|} \int_o^\infty \tau(\lambda)\rho_{\lambda 1} P_{s\lambda} \left[\sum_{i=1}^{4} c_i f\left(cos^{-1}\,\frac{r_i(\theta,\phi_\beta)}{2R}\right) + \frac{\rho_{\lambda 1} f_1}{1-\rho_\lambda}\right] d\lambda + n_\beta \tag{53}$$

$$\phi_\beta = cos^{-1}\left(1 - (1+\frac{h}{R})^2 sin^2\beta\right)^{\frac{1}{2}} - |\beta| \tag{54}$$

where β is the scan angle, (θ,ϕ_β) the elevation and azimuth angles of the corresponding scan point, ω_{FOV} the field-of-view of the scanner, $c_i P_{s\lambda}$ the spectral power of the i^{th} Tungsten source, and n_β the error in the corresponding measurement. Figure 2(b) shows plots of m normalized, while Figure 2(c) shows the actual measurements of the Shortwave ERBE Scanner instrument after corrections for electronic interference have been made. Note that both the shape (double hump) and the location of the peaks and valley on the sphere wall agree with the measured data.

From (35), it can be seen that another possible cause could be variations in $\rho_\lambda(\theta,\phi)$. However, this would necessitate that $\rho_\lambda(\theta,\phi)$ vary in a double hump manner, with its peaks occurring exactly at points opposite the light sources. This would be a rather unlikely coincidence, unless high levels of radiation have degraded the surface reflectivity

over a period of time. However, if the source is indeed diffuse, all portions of the sphere should degrade equally.

Temperature variations are an unlikely cause since the wall temperature is controlled, but particularly because the longwave scanner measurements show almost no variations.

The case of non-diffuse wall reflectance is the most difficult one to evaluate, as the expression for the radiance developed earlier (35) does not include this case. However, from qualitative considerations, it would appear that the peaks for this case would appear about halfway between the nadir point and the points opposite the light sources, if the sources are diffuse.

Loading Effects.

The geometry for ERBE non-scanning active cavity radiometers (ACR) when viewing the integrating sphere is shown in Figure 3. As opposed to the scanner geometry, the non-scanners are normally placed very close to the exit port to provide them with a wide field-of-view scene similar to that of Earth. This proximity, however, produces the loading effects discussed here. Since the surfaces of the non-scanners both emit and reflect radiation, the non-scanner acts as a source of radiation placed at the exit port. As this radiation would, in the no-load case, be lost through the exit port, the proximity of the non-scanner increases the amount of energy remaining in the sphere, and thus the irradiance measured by the instrument itself, and by the photo-diodes in the integrating sphere.

The main ACR surfaces seen by the integrating sphere are the active cavity, the base plate and the outer wall of the field-of-view limiter (FOVL). The active cavity effective area is small, and has practically no reflectance due to its surface properties and design geometry. The base plate is diffuse black, and reflects little energy. The FOVL outer wall has an aluminized mylar surface which is highly specular, so designed to minimize FOVL temperature variations due to outside sources when viewing the Earth. However, in the integrating sphere calibration, this surface can have considerable loading effects due to its high reflectivity.

Consider Figure 4 showing the exit port and the specular FOVL outer wall. Geometrical considerations show that of the radiation passing through the point (x, y), only those rays that are reflected from the crescent shown will reenter the sphere through the exit port. The crecent is obtained by excluding the rays that fall on the base plate from the circular area on the FOVL outer wall, with center at $(x/2, y/2)$. Thus, for a given point (x, y) on the exit port, the crescent surface is

$$A'(x,y) = \left[(x',y')|(x' - \frac{x}{2})^2 + (y' - \frac{y}{2})^2 \leq \frac{R^2}{4} \text{ and } x'^2 + y'^2 > R_1^2\right] \quad . \quad (55)$$

It is interesting to note that this reflecting crescent, $A'(x, y)$, is independent of the distance, h, between the instrument and the exit port. The dependence on this distance, hence the variation in loading, is due to the fact that, as h grows, the amount of radiation falling on the crescent (hence the reflected power) decreases. Thus, the loading effects are reduced as the distance of the instrument from the exit port increases, which is the expected trend.

It is important to note that another effect of loading by the ERBE non-scanners is the introduction of further non-uniformity of the wall surface. Even if the flashed opal glass produces perfectly diffuse radiation, the specular and highly reflecting FOVL outer wall will produce a brighter ring surrounding a less bright, roughly circular surface corresponding to the non-reflecting base plate, in the short wavelengths. Both the amount and the distribution of the bright areas will vary as the distance, h, varies. Such non-uniformities can produce differing measurement values for instruments with somewhat differing fields-of-view, such as the photo-diode and the ACR instrument itself.

In order to explain the behavior of some of the data obtained in the ERBE calibration chamber, it is of interest to estimate the magnitude of the loading effects. To this end, let $L_\lambda(x', y'; x, y)$ be the spectral radiance from the point (x, y) on the exit port to the point (x', y') on the FOVL outer wall. Then the spectral power $P_{\ell\lambda}$ reflected back into the sphere from the FOVL outer wall is

$$P_{\ell\lambda} = \rho_{\ell\lambda} \iint_{A_e} \iint_{A'(x,y)} L_\lambda(x', y'; x, y) \frac{\cos\chi \cos\chi'}{r^2} dA' \, dA \quad , \tag{56}$$

where $\rho_{\ell\lambda}$ is the spectral reflectivity of the FOVL outer wall, and A_e is the exit port surface.

Note that the loading effects can be considered a source entering through the exit port, in addition to the radiation entering through the entrance ports. The general solution obtained in the previous sections is valid for source radiation entering at any point, and with non-diffuse characteristics. Let $E_{\ell\lambda}(\theta, \phi)$ be the irradiance at (θ, ϕ) due to radiation reflected from the instrument at the exit port. $E_{\ell\lambda}(\theta, \phi)$ will be zero outside the area A_ℓ on the sphere, and, due to the geometry, A_ℓ will be a subset of the sphere wall, A_1. From (34), the spectral power, $P_{\lambda 5}$, leaving through the exit port A_5 is

$$P_{\lambda 5} = \iint_{A_5} E_{s\lambda}(\theta, \phi) dA + \frac{|A_5|}{(1 - \bar{\rho}_\lambda)|A_s|} \left[\iint_{A_s} \rho_\lambda(\theta', \phi') [E_{s\lambda}(\theta', \phi') + E_{\ell\lambda}(\theta', \phi')] dA' + E_{e\lambda} |A_s| \right] \quad , \tag{57}$$

$$\iint_{A_s} \rho_\lambda(\theta', \phi') E_{\ell\lambda}(\theta', \phi') dA' = \rho_{\lambda 1} \iint_{A_\ell} E_{\ell\lambda}(\theta', \phi') dA' = \rho_{\lambda 1} P_{\ell\lambda} \tag{58}$$

Define G_λ as the ratio

$$G_\lambda = P_{\ell\lambda} / \rho_{\ell\lambda} (P_{\lambda 5} - |A_5| \bar{E}_{s\lambda 5}) \tag{59}$$

Substituting (58) and (59) into (57) and solving for $P_{\lambda 5}$,

$$P_{\lambda 5} = \frac{f_5}{1 - \bar{\rho}_\lambda - f_5 G_\lambda \rho_{\ell\lambda} \rho_{\lambda 1}} \left[\iint_{A_s} \rho_\lambda(\theta', \phi') E_{s\lambda}(\theta', \phi') dA' + |A_s| E_{e\lambda} \right] + |A_5| \bar{E}_{s\lambda 5} \tag{60}$$

$$P_{\ell\lambda} = \rho_{\ell\lambda} G_\lambda (P_{\lambda 5} - |A_5| \bar{E}_{s\lambda 5}) \tag{61}$$

Including emitted loading effects as an additional source of radiation

$$P_{\lambda 5} = \frac{f_5}{1 - \bar{\rho}_\lambda - f_5 G_\lambda \rho_{\ell\lambda} \rho_{\lambda 1}} \left[\iint_{A_s} \rho_\lambda(\theta', \phi') E_{s\lambda}(\theta', \phi') dA' + |A_s| E_{e\lambda} + \iint_{A_s} \rho_\lambda(\theta', \phi') E_{\ell_s \lambda}(\theta', \phi') dA' \right] + |A_5| \bar{E}_{s\lambda 5} \tag{62}$$

where $E_{\ell_s \lambda}(\theta, \phi)$ is the irradiance due to emitted energy from the load or measuring instrument.

Thus, the spectral power, $P_{\lambda 5}$, leaving through the exit port A_5 including non-uniform loading effects from reflection and emission is given by (62). It is interesting to note that while the emission from the load introduces an additive term (i.e., the last term in (62)), the reflection from the load, as might be expected, modifies the average sphere spectral reflectivity $\bar{\rho}_\lambda$.

$$\hat{\rho}_\lambda = \bar{\rho}_\lambda + f_5 G_\lambda \rho_{\ell\lambda} \rho_{\lambda 1} = \sum_{k=1}^{4} f_k \rho_{\lambda k} + f_5 G_\lambda \rho_{\ell\lambda} \rho_{\lambda 1} \quad , \tag{63}$$

where G_λ varies with the distance, h, between the load and the sphere. Also note that the presence of $\rho_{\lambda 1}$ in the last term of (63) is due to the non-uniformity of the specular reflections ($A_\ell \subset A_1$), and the fact that the FOVL outer wall is flat rather than spherical; i.e., $E_{\ell\lambda}(\theta, \phi) = 0, (\theta, \phi) \epsilon A_5$. From (34), after some manipulation we have

$$E_\lambda(\theta, \phi) = E_{s\lambda}(\theta, \phi) + E_{\ell\lambda}(\theta, \phi) + \frac{1}{(1 - \hat{\rho}_\lambda)|A_s|} \left[\iint_{A_s} \rho_\lambda(\theta', \phi') E_{s\lambda}(\theta', \phi') dA' + |A_s| E_{e\lambda} + \iint_{A_s} \rho_\lambda(\theta', \phi') E_{\ell_s \lambda}(\theta', \phi') dA' \right] \quad . \tag{64}$$

To obtain an approximate value for G_λ, suppose that $E_{\ell\lambda}$ is equally distributed over the sphere wall surface A_ℓ. Then after some manipulation,

$$G_\lambda \simeq \frac{\rho_{\lambda 1} + \frac{\bar{E}_{s\lambda 1}}{\tilde{E}_{\lambda 5}}\rho_{\lambda 1} + \frac{\epsilon_{\lambda 1} L_B(\lambda, T_1)}{\tilde{E}_{\lambda 5}}}{1 - \frac{\rho_{\lambda 1}\rho_{\ell\lambda} H}{|A_\ell|}} \frac{H}{\pi |A_5|} \approx \frac{H}{\pi |A_5|} \quad . \tag{65}$$

$$H = \iint_{A_s} \iint_{A'(x,y)} \frac{\cos\chi \cos\chi'}{r^2} dA' \, dA \quad . \tag{66}$$

Due to the geometry of $A'(x,y)$, the exact value of H is difficult to obtain; however, after considerable manipulation, an approximate value can be shown to be

$$H \approx \pi^2 (R^2 - R_1^2) \left[1 - \frac{5}{u} ln\,(1 + \frac{u}{5}) + \frac{1}{2u} \left(ln \frac{(1 + \frac{4u}{5})^2}{(1+u)} + 4\, ln \frac{(1 + \frac{u}{20})^2}{(1 + \frac{u}{4})} \right) \right] \tag{67}$$

$$u = \frac{r^2 - R_1^2}{h^2} \quad , \tag{68}$$

where R is the radius of the exit port and R_1 is the radius of the FOV opening.

To see the magnitude of the loading effect, consider a shortwave measurement of the irradiance of the form

$$m(h) = K \int_{\lambda_1}^{\lambda_2} \frac{1/|A_s|}{1 - \bar{\rho}_\lambda - f_5 \rho_\lambda \rho_{\ell\lambda} G_\lambda(h)} \iint_{A_s} \rho_\lambda(\theta', \theta') E_{s\lambda}(\theta', \phi') dA' d\lambda \tag{69}$$

Figure 5(a) shows a plot of the normalized measurement $m(h)/m(h_o)$ as a function of the distance, h, of the ACR from the sphere for the ERBE Wide-Field-Of-View (WFOV) Total channel, using $\lambda_1 = .6\mu m, \lambda_2 = .9\mu m$, and estimates of the spectral reflectance, source spectral power and geometry for the ERBE integrating sphere. As can be seen from this plot, the magnitude of the loading effects in the shortwave band can be as much

as 13 % of the no-load condition at the closest point h_o. The effect tends to diminish in roughly an exponential decay shape. It is important to note that the magnitude of the loading effects is extremely dependent on the wall spectral reflectivity when it is close to unity.

Figure 5(b) shows a plot of the sphere loading effects when the ERBE Medium-Field-Of-View (MFOV) Total channel is placed at the exit port. As can be seen from the plot, the MFOV loading can be as much as 16.9 % of the no-load condition for shortwave radiation. The higher loading is caused by the fact that MFOV channel has a larger area FOVL outer wall, which reduces the sensor's FOV. Thus, for shortwave measurements, a difference of about 4 % may be expected between WFOV and MFOV loading.

The loading effects for emitted longwave radiation can also be computed using

$$m(h) = K \int_o^\infty \frac{1}{a - \bar{\rho}_\lambda - f_5 \rho_{\lambda 1} \rho_{\ell\lambda} G_\lambda(h)} \left[E_{e\lambda} + \frac{1}{|A_s|} \iint_{A_s} \rho_\lambda(\theta', \phi') E_{\ell_s \lambda}(\theta', \phi') dA' \right] \quad . \tag{70}$$

The loading effect for emitted radiation can be considerably lower than for shortwave radiation, due to the fact that the spectral reflectance is considerably lower at these wavelengths. Also note the presence of an extra term for emission from the ACR, in (70). Neglecting the effect of the active cavity due to its small area, (70) can be rewritten as

$$m(h) = K \int_o^\infty \frac{f_1 \epsilon_{\lambda 1} L_B(\lambda, T_1) + f_2 \epsilon_{\lambda 2} L_B(\lambda, T_2) + f_e \rho_{\lambda 1} \epsilon_{\ell\lambda} L_B(\lambda, T_\lambda) F(h)}{1 - \bar{\rho}_\lambda - f_5 \rho_{\lambda_1} \rho_{\ell\lambda} G_\lambda(h)} \, d\lambda \,, \tag{71}$$

where $F(h)$ is the configuration factor from the FOV aperture to the exit port.

Reliable spectral reflectance and emittance data in the longwave band being currently unavailable, reliable prediction of this loading effect is not possible. However, the longwave loading effects are one or more orders of magnitude lower than the shortwave loading effects.

Calibration of Photo-Diodes.

Since the ERBE ACR's are meticulously calibrated using the MRBB, it is possible to calibrate the integrating sphere photo-diodes using the total wavelength ACR channels. The basic procedure used for this purpose was to measure the sphere output with the lamps on, then with the lamps off, using the total ACR channels and a photo-diode. The difference between the lamps on versus lamps off measurements for each sensor were taken as measurements of the shortwave sphere output. This procedure resulted in a nonlinear (quadratic) relationship between the photo-diode and ACR readings. Another finding was that the relationship of the photo-diode to the MFOV output was different than the relationship to the WFOV output.

The "apparent" non-linearity of the photo-diode may be, at least partially, explained by the following observation. Assuming a uniform wall radiance, the non-scanner measurement can be approximated by

$$E(E_s) = \int_o^\infty \frac{f_1 \rho_{\lambda 1} \bar{E}_{s\lambda 1}}{1-\hat{\rho}_\lambda}\, d\lambda + \frac{f_1 \epsilon_1 \sigma T_1^4 + f_2 \epsilon_2 T_2^4 + f_e F \rho_{\lambda_e 1} \epsilon_\ell \sigma T_\ell^4}{1-\hat{\rho}_{\lambda_e}} \quad , \tag{72}$$

where the second term must use longwave values for $\hat{\rho}_{\lambda_e}, \rho_{\lambda_e 1}$. The difference between the lamps on and off measurements is

$$\Delta E = E(E_s) - E(0) = \int_o^\infty \frac{f_1 \rho_{\lambda 1} E_{s\lambda 1}}{1-\hat{\rho}_\lambda}\, d\lambda + \sigma \frac{f_1 \epsilon_1 (T_1^4 - T_{10}^4) + f_2 \epsilon_2 (T_2^4 - T_{20}^4) + f_e F \rho_{\lambda_e 1} \epsilon_\ell (T_\ell^4 - T_{\ell 0}^4)}{1-\hat{\rho}_{\lambda_e}} \quad , \tag{73}$$

where $T_{10}, T_{20}, T_{\ell 0}$ denote the temperatures when the lamps are off. From (73), it is clear that some emitted radiation may be present in ΔE. Whereas the wall temperature T_1 is controlled and measured, the temperature of the flashed opal diffuser glass, T_2, is neither

controlled nor measured. Due to some absorption, T_2 can be considerably higher with the lamps on than off.

To see if this term is negligible or not, suppose that initially, the opal glass is at the sphere wall temperature of $-13°C$, and that it heats up to a temperature of $60°C$ when the lamp has been on for a period of time. For perfect emission, the magnitude of this term is $3W/m^2$ for $\hat{\rho}_{\lambda_s} = .1$, and $4.3W/m^2$ for $\hat{\rho}_{\lambda_s} = .4$. Thus, if the opal glass temperature reaches such temperatures or higher ones, the effect of the term $f_2\epsilon_2\sigma(T_2^4 - T_{20}^4)/1 - \hat{\rho}_{\lambda_s}$ cannot be neglected.

Thus, if the photo-diode measurement is directly proportional to the shortwave source output represented by the first term in (73),

$$\Delta E = g\,\Delta V + \Delta E_\ell + n \tag{74}$$

where ΔE_ℓ is the emitted energy with the lamps on which was not present with the lamps off, ΔV is the photo-diode reading and n is the combined error in the instrument readings. Clearly, if the longwave term is not taken into account, the relationship between ΔE and ΔV would appear to be nonlinear.

It should be noted that ΔE_ℓ is dependent on the sphere wall temperature, T_2, since the heat being conducted from the opal glass to the sphere wall (through the insulator) depends on the wall temperature.

Table 1 shows ground calibration data obtained by placing the ERBE WFOV Total Waveband instrument at the integrating sphere exit port, when the sphere wall temperature varied between $-10.08°C$ and $-13.15°C$. The data was obtained using the various (3) levels of reference cavity heating (calibration heater voltage). A linear fit to the data of the type shown in (74) is also shown in Table 1. As can be seen, the linear curve fits the data very closely*, well within the accuracy of the instrument, indicating the validity of the theoretical predictions. These results point to a more satisfactory explanation of

*Note that two points of apparently inconsistent data (e.g., higher SiPd reading corre-

the calibration data by producing a linear photo-diode response to shortwave radiation, coupled with some undesired longwave radiation due to the heating of the opal glass diffuser when the lamps are turned on. The amount of extra emitted radiation is also within expectation.

From the ground calibration data shown using the ERBE integrating sphere, the accuracy of the ERBE WFOV Total Wave-band instrument to a wide field- of-view shortwave scene similar to what might be encountered in looking at the Earth corresponds to an error with a standard deviation of $.73\,W/m^2$, which indicates an extremely accurate instrument from this initial analysis.

Long-Wave Output of the Integrating Sphere.

Another unexpected effect observed in the calibration data is that ERBE Non-scanner instruments measure a larger long-wave irradiance output from the sphere than the measured sphere wall temperature can provide with lamps off. For the WFOV case, the wall temperature would have to be $2.45°C$ higher than that measured to account for this difference of about $10\,W/m^2$. This temperature difference is too large to be explained by errors in the measured wall temperature. Furthermore, due to the high accuracy of the WFOV instrument as evidenced by its MRBB calibration results, it is reasonable to expect that the sphere long-wave output is in fact larger than originally expected.

As discussed earlier, while loading effects tend to increase the sphere output, the magnitude of the longwave loading is too small to explain the observed difference. However, loading does produce a small effect in the right direction, and may partially explain differences between instruments.

As observed earlier, it is reasonable to expect that the opal glass diffuser temperature at the entrance port increases when the lamps are on. On the other hand, the measurements considered are taken with the lamps off. However, observation of the time log shows that

sponding to lower irradiance), probably due to transients and noise, account for most of the error.

the lamps-off readings are generally taken a few minutes after the lamps-on readings. As the opal glass is surrounded by the insulator (see Fig. 6) which contacts the sphere wall, this may not be sufficient time to cool the opal glass and insulator by radiation nor conduction. So that, when the lamps-off readings are taken, the temperature of the diffuser assembly may still be quite high. An approximate estimate of the diffuser time constant is about 400 seconds; i.e., after 400 seconds, the diffuser temperature is down by only 36 %. A conservative estimate of the lamps-on steady-state diffuser temperature is about $200°C$. At this temperature, the diffuser assembly would contribute about $12 W/m^2$ to the sphere output. Whether or not the extra $10 W/m^2$ is caused by the high temperature of the diffuser assembly, the effect is not negligible, and should be incorporated in any calculations of the emitted sphere output. Furthermore, if the opal glass and insulator reach temperatures approaching $200°C$, the portions of the sphere wall near them are likely to be at higher temperatures than the measured wall temperature due to radiative and conductive effects. These portions of the wall would then also emit at higher than expected levels.

MFOV Shortwave Calibration.

The shortwave calibration of the ERBE MFOV Total Waveband channel can be achieved with the same procedure used in the shortwave calibration of the WFOV channel. As with the WFOV calibration, the relationship between the MFOV and photo-diode reading is of the form of (74). However, the ground calibration data shows that for the same photo-diode reading, the MFOV channel measures a higher irradiance than the WFOV channel. This implies that the photo-diode reading cannot be used independently of the instrument at the exit port. The main reason for this behavior is the non-uniformity of the sphere wall, aggravated by non-uniform loading, coupled with the different fields-of-view of the MFOV, WFOV and photo-diodes.

The exact manner in which the wall non-uniformity can cause this behavior can be seen by combining (64), (36) and (9) to obtain the MFOV measurement including a non-

uniform wall.

$$m^M = \int_o^\infty (\bar{E}_{s\lambda}^M + \bar{E}_{\ell\lambda}^M)d\lambda + f_1 \int_o^\infty \frac{\rho_{\lambda 1}^2}{1-\hat{\rho}_\lambda^M} \bar{E}_{s\lambda 1} d\lambda$$
$$+ \left(\frac{S_1^M}{S^M} + \frac{f_1 \rho_{\lambda_e 1}}{1-\hat{\rho}_{\lambda_e}^M}\right)\epsilon_1 \sigma T_1^4 + \left(\frac{S_2^M}{S^M} + \frac{f_2 \rho_{\lambda_e 1}}{1-\hat{\rho}_{\lambda_e}^M}\right)\epsilon_2 \sigma T_2^4$$
$$+ \frac{f_e F^M \rho_{\lambda_e 1}^2}{1-\hat{\rho}_{\lambda_e}^M}\epsilon_\ell \sigma T_\ell^4 + n^M \quad , \tag{75}$$

$$\bar{E}_s^M = \frac{1}{S^M} \iint_{A_e} S^M(\theta,\phi)\rho_\lambda(\theta,\phi) E_{s\lambda}^M(\theta,\phi) dA \quad , \tag{76}$$

$$\bar{E}_{\ell\lambda}^M = \frac{1}{S^M} \iint_{A_e} S^M(\theta,\phi)\rho_\lambda(\theta,\phi) E_{\ell\lambda}^M(\theta,\phi) dA \quad , \tag{77}$$

$$S^M = \iint_{A_e} S^M(\theta,\phi) dA \quad , \tag{78}$$

where the superscript M denotes the MFOV instrument; note that the same expression is applicable to the WFOV instrument when the corresponding response is used. On the other hand, the photo-diode reading can be expressed by

$$m^P = K\left[\int_{\lambda_1}^{\lambda_2} (\bar{E}_{s\lambda}^P + \bar{E}_{\ell\lambda}^P)d\lambda + f_1 \int_{\lambda_1}^{\lambda_2} \frac{\rho_{\lambda 1}^2}{1-\hat{\rho}_\lambda} \bar{E}_{s\lambda 1} d\lambda\right] + n^P \tag{79}$$

where the loading related terms $\hat{\rho}_\lambda$ and $\bar{E}_{\ell\lambda}^P$ depend on the particular instrument at the exit port when the photo-diode reading is taken.

First note that, if the source irradiance and wall reflectivity are uniform, then

$$\bar{E}_{s\lambda}^M = \bar{E}_{s\lambda}^W = \rho_{\lambda 1} E_{s\lambda} \tag{80}$$

even though non-uniform loading effects will still be present. However, due to the known non-uniformities on the wall (80) does not hold. If the source's spectral and directional characteristics remain constant while its intensity varies, then

$$m^M = g^M m^{P/M} + E_\ell^M + n_1 \quad , \tag{81}$$

$$m^W = g^W m^{P/W} + E_\ell^W + n_2 \quad , \tag{82}$$

Since $\bar{E}_{s\lambda}^M + \bar{E}_{\ell\lambda}^M > \bar{E}_{s\lambda}^W + \bar{E}_{\ell\lambda}^W$ due to the non-uniformities, it may be expected that $g^M > g^W$.

$$\Delta m^M = g^M \Delta m^{P/M} + \Delta E_\ell^M + \Delta n_1 \quad . \tag{83}$$

As the longwave loading effects are relatively small, $\Delta E_\ell^M \approx \Delta E_\ell^W$.

Table 2 shows ground calibration data with the ERBE MFOV Total Waveband instrument at the exit port with the wall temperature varying from $-10.5°C$ to $-13°C$. The linear fit

$$\Delta m^M = 34.42\, \Delta m^{P/M} + 2.3 + \Delta n_1 \quad , \tag{84}$$

results in an uncertainty or error with standard deviation $1.5\, W/m^2$. This uncertainty is less than the uncertainty in the MFOV instrument noise. Thus, the integrating sphere shortwave calibration of the MFOV instrument is consistent with its longwave MRBB calibration.

IV. CONCLUSIONS

In this paper, the general solution of the spectral radiance and the spectral radiant incidence for a spherical cavity with diffuse reflectivity are obtained analytically by solving a Fredholm equation of the 2^{nd} kind. Some previous results are easily obtained from these expressions as special cases. The solution is applicable to spheres with non-uniform and non-diffuse input source radiation, containing an arbitrary number of openings or ports of any size and shape, with non-uniform spectral reflectivity, directional spectral emissivity and temperature distribution on the sphere wall.

A general measurement equation is obtained to describe the output of a sensor measuring the output of the spheres at the exit port. The measurement equation accommodates an arbitrary sensor field-of-view determined by the sensor's point spread function and spectral response.

The results obtained are applied to the Earth Radiation Budget Experiment (ERBE) integrating sphere. The sphere wall uniformity, the loading effects due to the presence of the measuring sensor, and non-uniform wall temperature effects are investigated. It is shown that using an appropriate interpretation and processing of the data, a high-accuracy shortwave calibration of the ERBE sensors can be achieved.

ACKNOWLEDGMENTS. The authors would like to thank Dr. Sang H. Choi of ICS for stimulating discussions on the temperature of the opal diffuser.

REFERENCES

1. Sumpner, W. E., "The Diffusion of Light," *Phys. Soc. Proc. 12,* 10, 1892.
2. Ulbricht, R., "Photometer for Mean Spherical Candle-Power," *E. T. Z. 21,* 595, 1900.
3. Steinmetz, C. P., *Radiation, Light and Illumination,* p. 184, McGraw-Hill Book Co., 1901.
4. Hardy, A. C., and O. W. Pineo, "The Errors Due to the Finite Size of Holes and Samples in Integrating Spheres," *J. Opt. Soc. Am. 21,* 502, 1931.
5. Walsh, J. W. T., *Photometry,* Constable & Co. Ltd., 1926.
6. Goebel, D. G., "Generalized Integrating-Sphere Theory," *Appl. Opt. 6,* 125, 1967.
7. Lovell, D. J., "Instrumentation to Assess Interferometer Performance," *SPIE Proc. 191,* 143, 1979.
8. Van den Akker, J. A., Dearth, L. R., and W. M. Shillcox, "Evaluation of Absolute Reflectance for Standardization Purposes," *J. Opt. Soc. Am. 56,* 250, 1966.
9. Goebel, D. G., Caldwell, B. P., and H. K. Hammond, III, "Use of an Auxiliary Sphere with a Spectroreflectometer to Obtain Absolute Reflectance," *J. Opt. Soc. Am. 56,* 783, 1966.
10. Hovis, W. A., and J. S. Knoll, "Characteristics of an Internally Illuminated Calibration Sphere," *Appl. Opt. 22,* No. 24, 4004, 1983.
11. Lovell, D. J., "Theory and Applications of Integrating Sphere Technology," *Laser Focus/Electro-Optics,* 86, 1984.
12. Barkstrom, B. R., and J. B. Hall, Jr., "Earth Radiation Budget Experiment (ERBE): An overview," *J. Energy 6,* No. 2, 1982.
13. Barkstrom, B. R., and G. L. Smith, "The Earth Radiation Budget Experiment: Science and Implementation," *Reviews of Geophysics 24,* No. 2, pp. 379-390, 1986.

14. Carman, S. L., and R. J. Hesser, "An Integrating Sphere as a Precision Radiometric Calibration Source," *Proc. SPIE 416,* 1983.

15. Falbel, A., and A. Iannarelli, "Radiometric Calibration for the Earth Radiation Budget Experiments," *Proc. SPIE,* 1981.

16. Luther, M. R., Cooper, J. E., and G. R. Taylor, "The Earth Radiation Budget Experiment Nonscanner Instrument," *Reviews of Geophysics 24,* No. 2, pp. 391-399, 1986.

17. Kopia, L. P., "Earth Radiation Budget Experiment Scanner Instrument," *Reviews of Geophysics 24* No. 2, pp. 400-406, 1986.

18. Moon, P., "On Interreflections," *J. Opt. Soc. Am. 30,* 195, 1940.

19. Jacquez, J. A., and H. F. Kuppenheim, "Theory of the Integrating Sphere," *J. Opt. Soc. Am. 45,* No. 6, 460, 1955.

20. Jensen, H. H., "Some Notes on Heat Transfer by Radiation," *Kgl. Danske Videnskab. Selskab. Mat.-Fys. Medd. 24,* No. 8, 1, 1948.

21. Sparrow, E. M., and V. K. Jonsson, "Absorption and Emission Characteristics of Diffuse Spherical Enclosures," *NASA* TN D-1289, 1962.

22. Siegel, R., and J. R. Howell, *Thermal Radiation Heat Transfer,* pp. 271-273, McGraw-Hill Book Co., 1981.

23. Sparrow, E. M., and R. D. Cess, *Radiation Heat Transfer,* pp. 174-179, McGraw-Hill Book Co., 1978.

24. Hisdal, B. J., "Reflectance of Perfect Diffuse and Specular Samples in the Integrating Sphere," *J. Opt. Soc. Am. 55,* No. 9, 1122, 1965.

25. Hisdal, B. J., "Reflectance of Nonperfect Surfaces in the Integrating Sphere," *J. Opt. Soc. Am. 55,* No. 10, 1255, 1965.

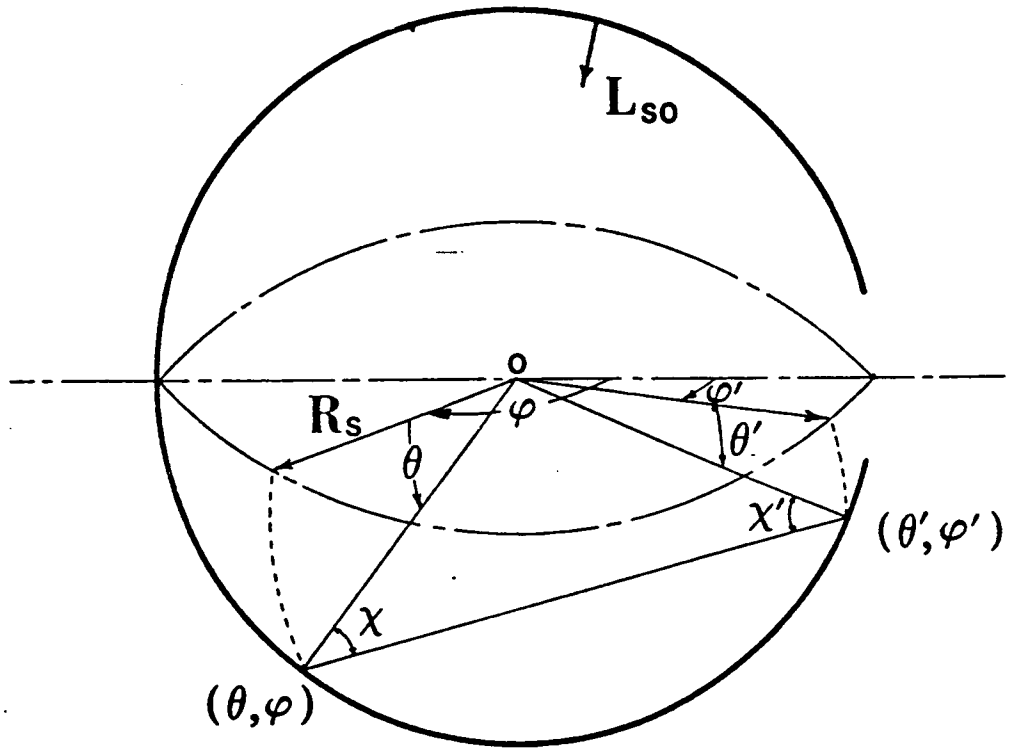

FIGURE 1(B). DEFINITION OF ANGLES ON SPHERE SURFACES

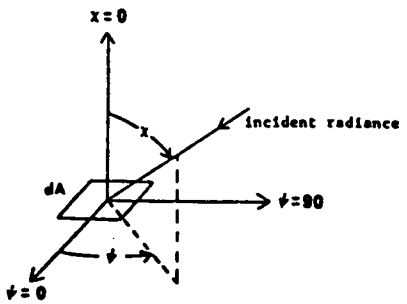

FIGURE 1(A). DEFINITION OF GEOMETRIC QUANTITIES

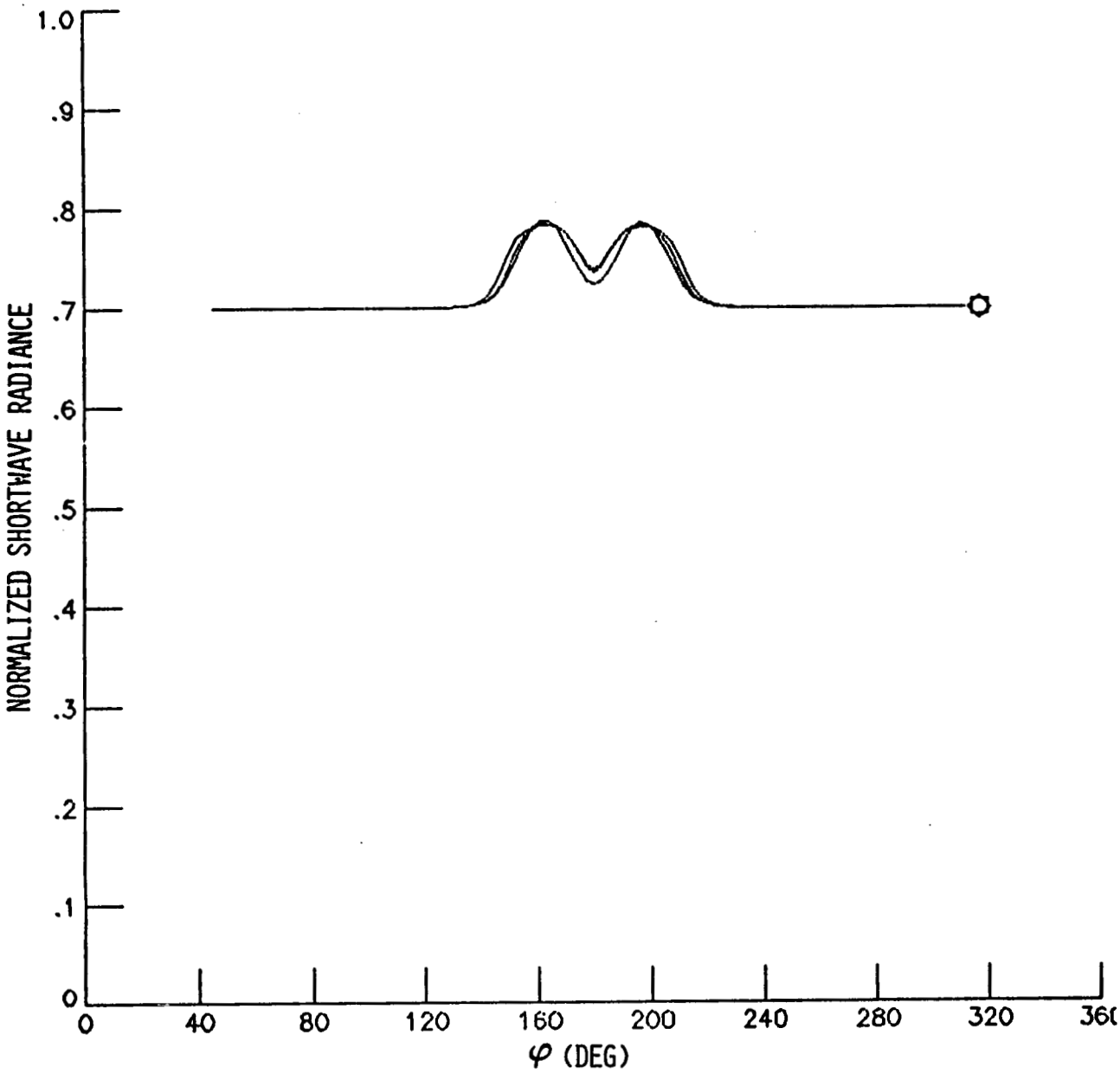

FIGURE 2(A). IMPERFECT OPAL GLASS DIFFUSER EFFECTS ON INTEGRATING SPHERE WALL UNIFORMITY ($\theta = 0, \pm 5°$)

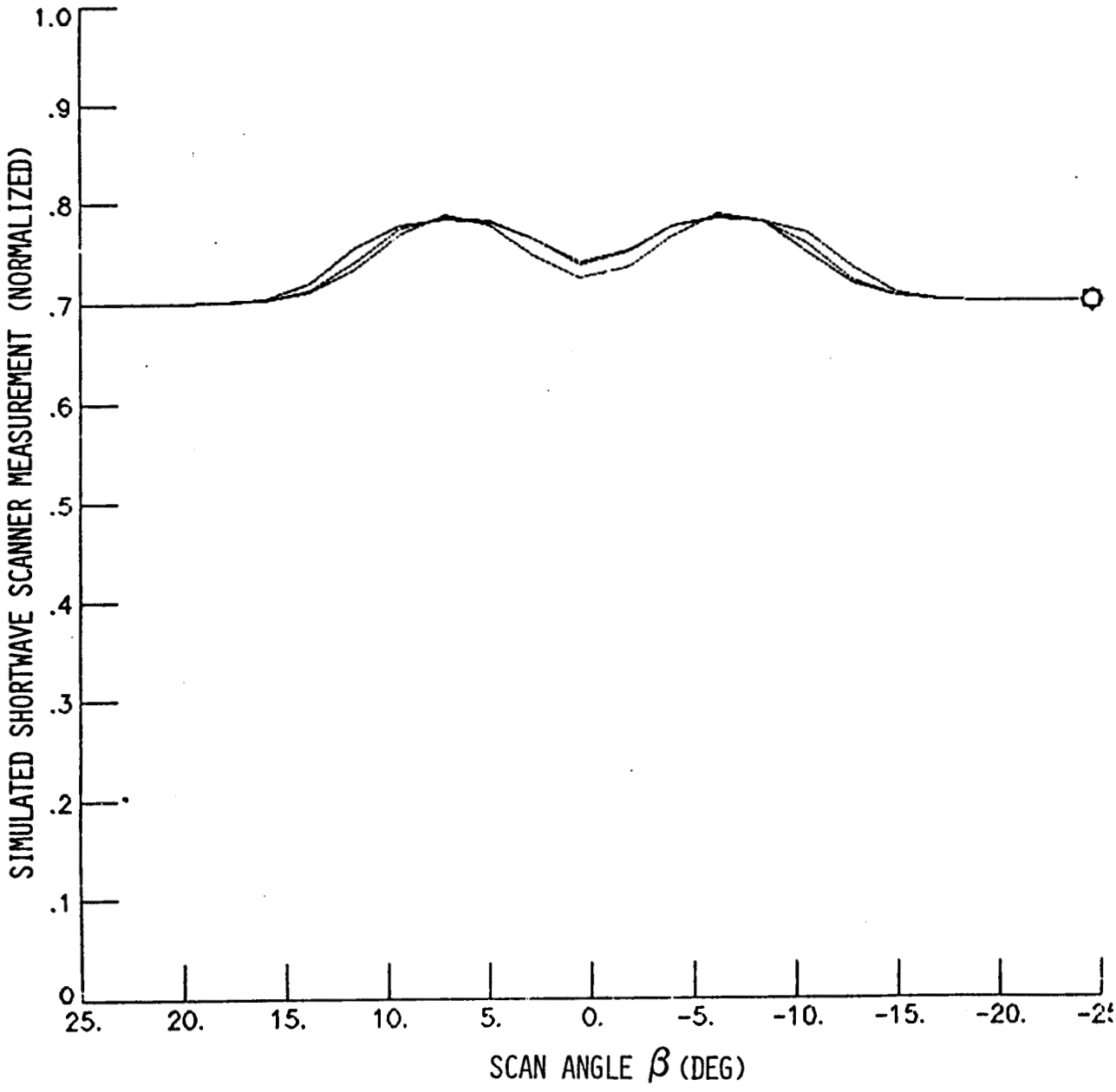

FIGURE 2(B). IMPERFECT OPAL GLASS DIFFUSER EFFECTS ON INTEGRATING SPHERE WALL UNIFORMITY ($\theta = 0, \pm 5°$)

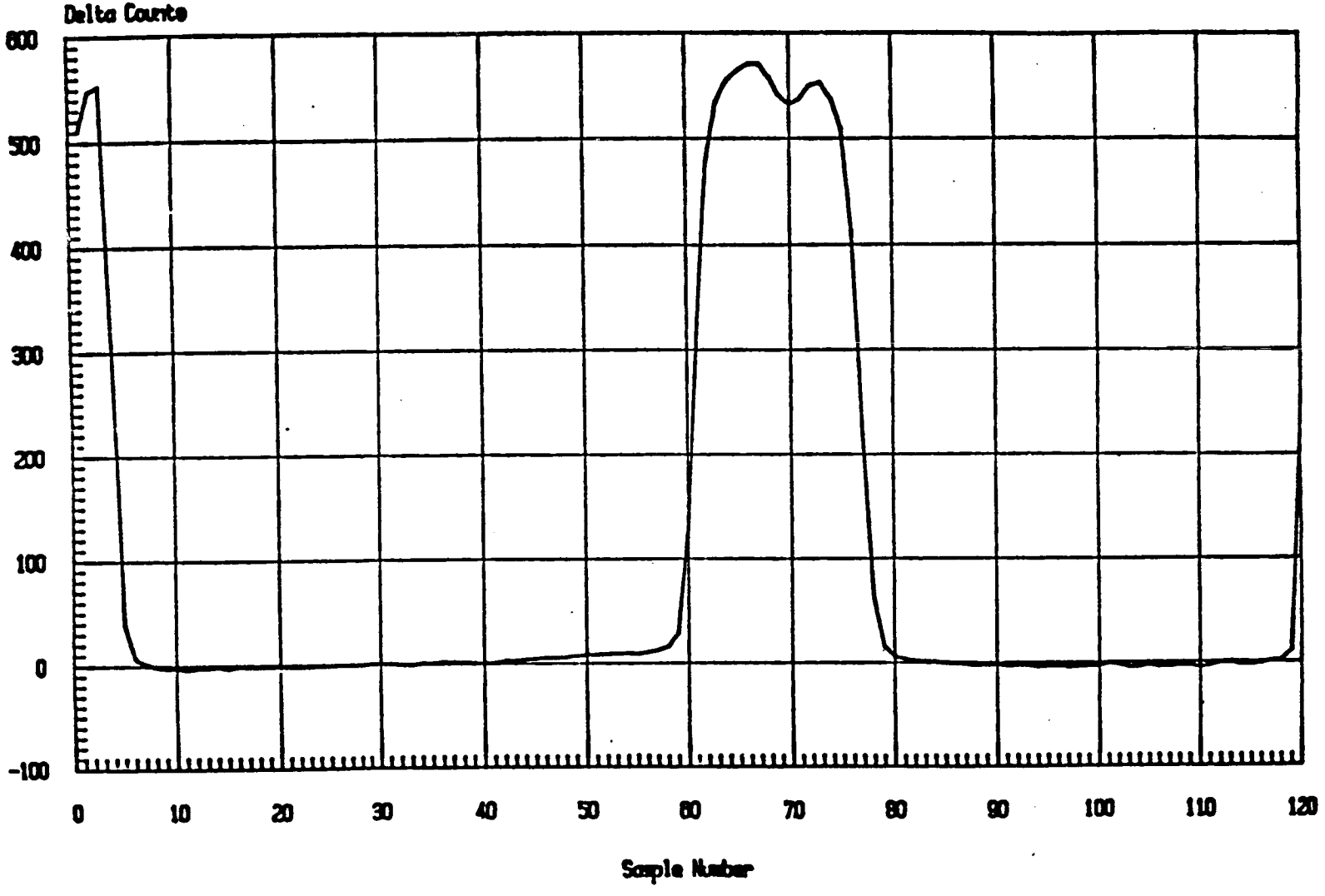

FIGURE 2(C). SHORTWAVE SCANNER OUTPUT SCANNING INTEGRATING SPHERE

Key

(1) Integrating Sphere Inner Wall

(2) Outer Wall of ACR Field-of-View Limiter

(3) Baseplate of Active Cavity Radiometer

(4) Active Cavity of Radiometer

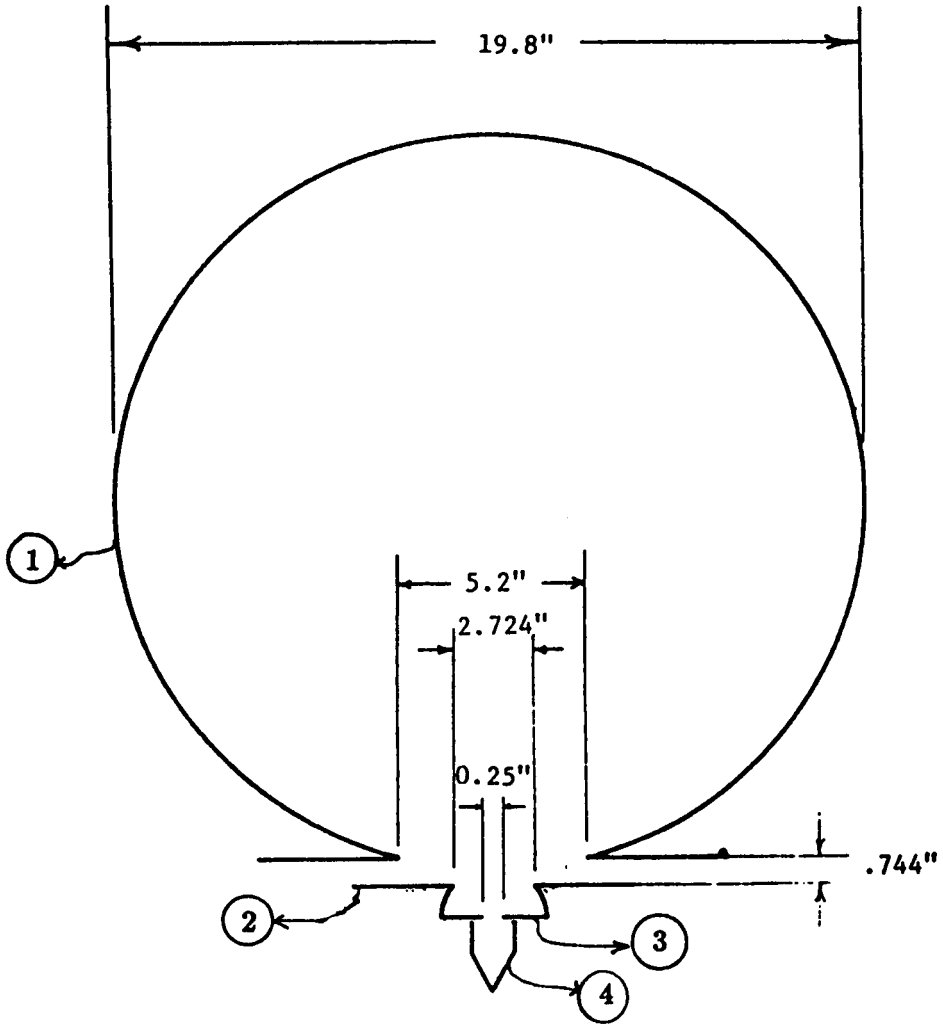

FIGURE 3. GEOMETRY OF ERBE NON-SCANNER INSTRUMENT AT INTEGRATING SPHERE EXIT PORT

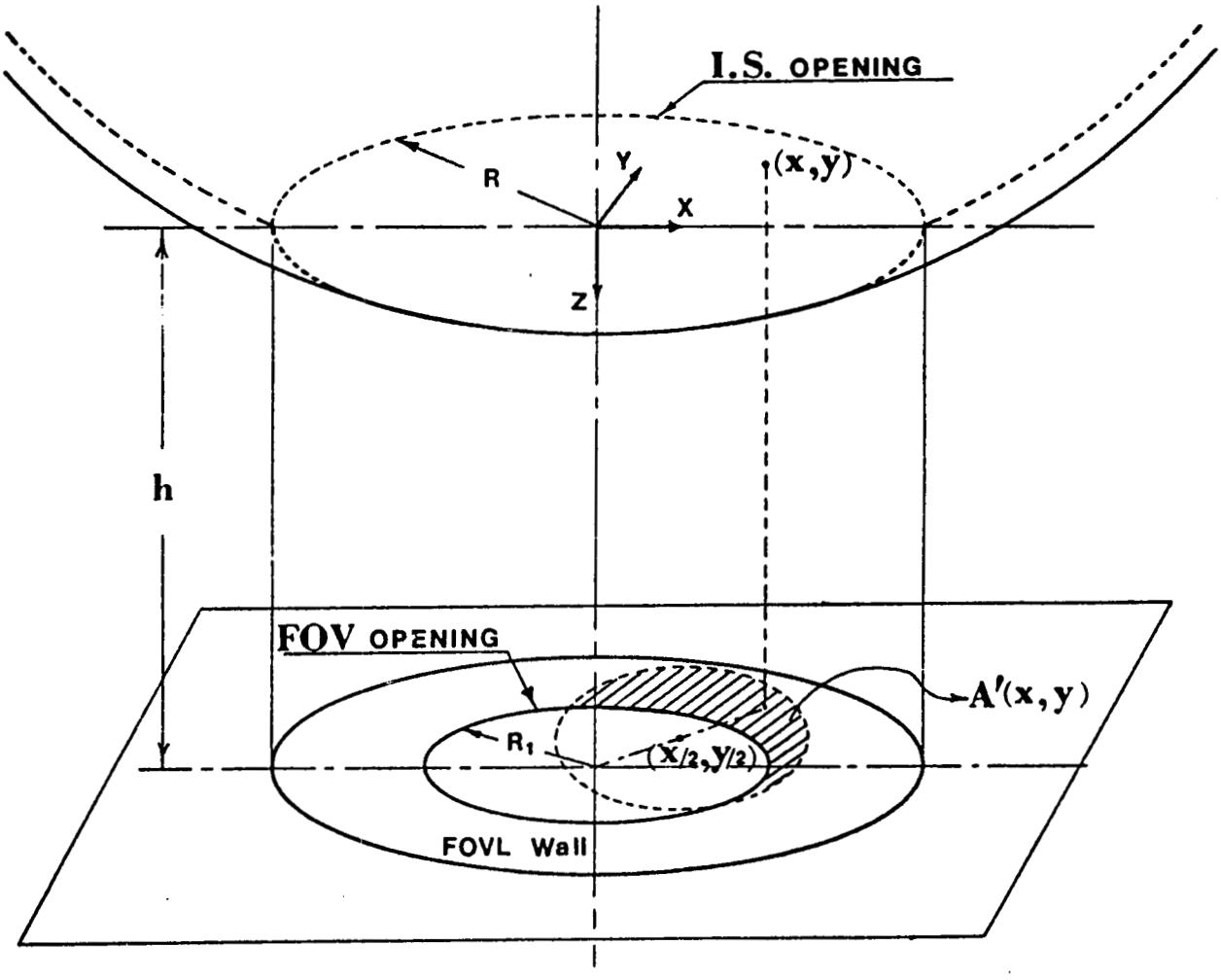

FIGURE 4. LOADING EFFECTS DUE TO SPECULAR FOVL OUTER WALL

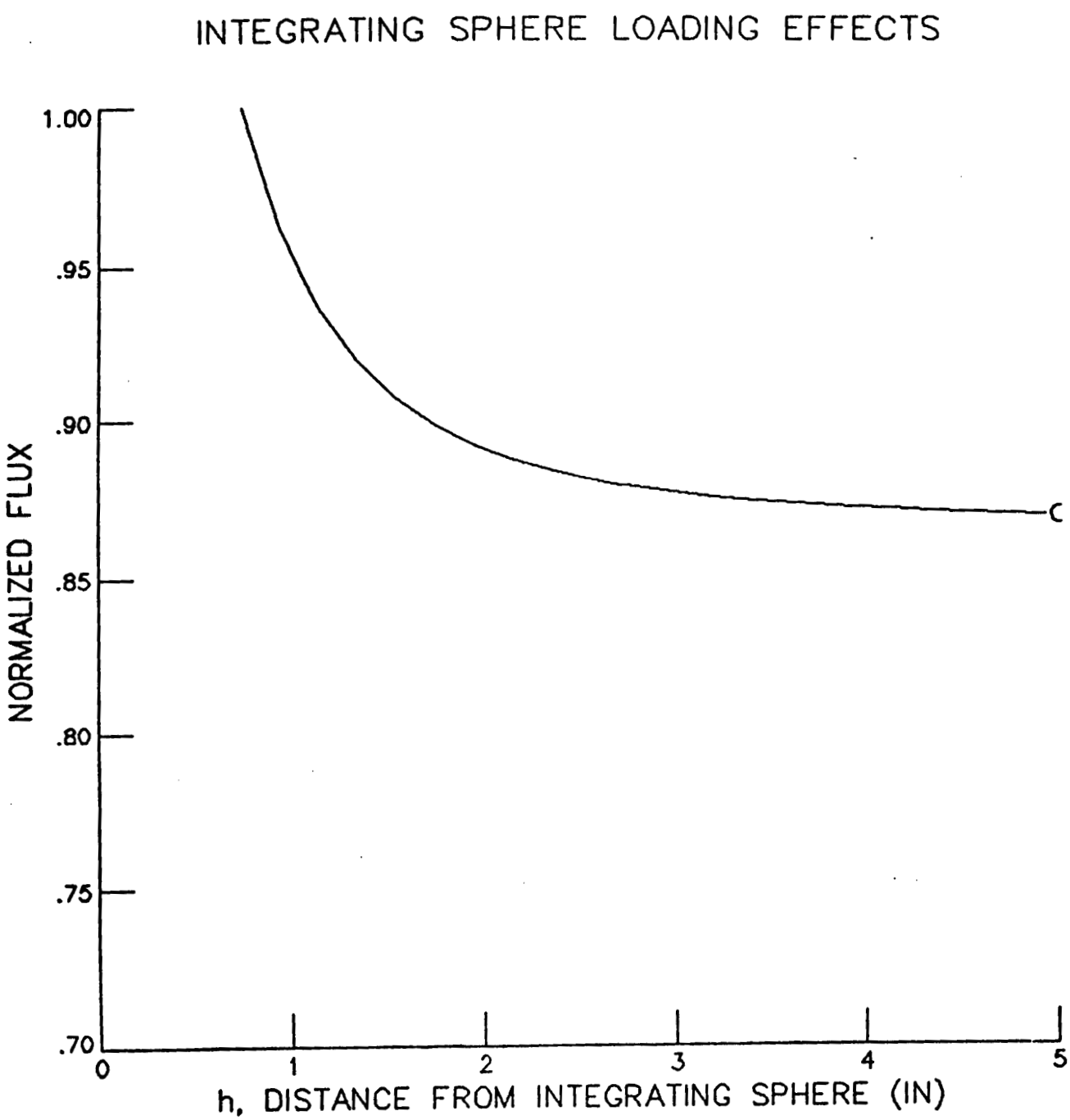

FIGURE 5(A). SHORTWAVE LOADING EFFECTS FOR THE WFOV TOTAL INSTRUMENT ($h_o = .744"$)

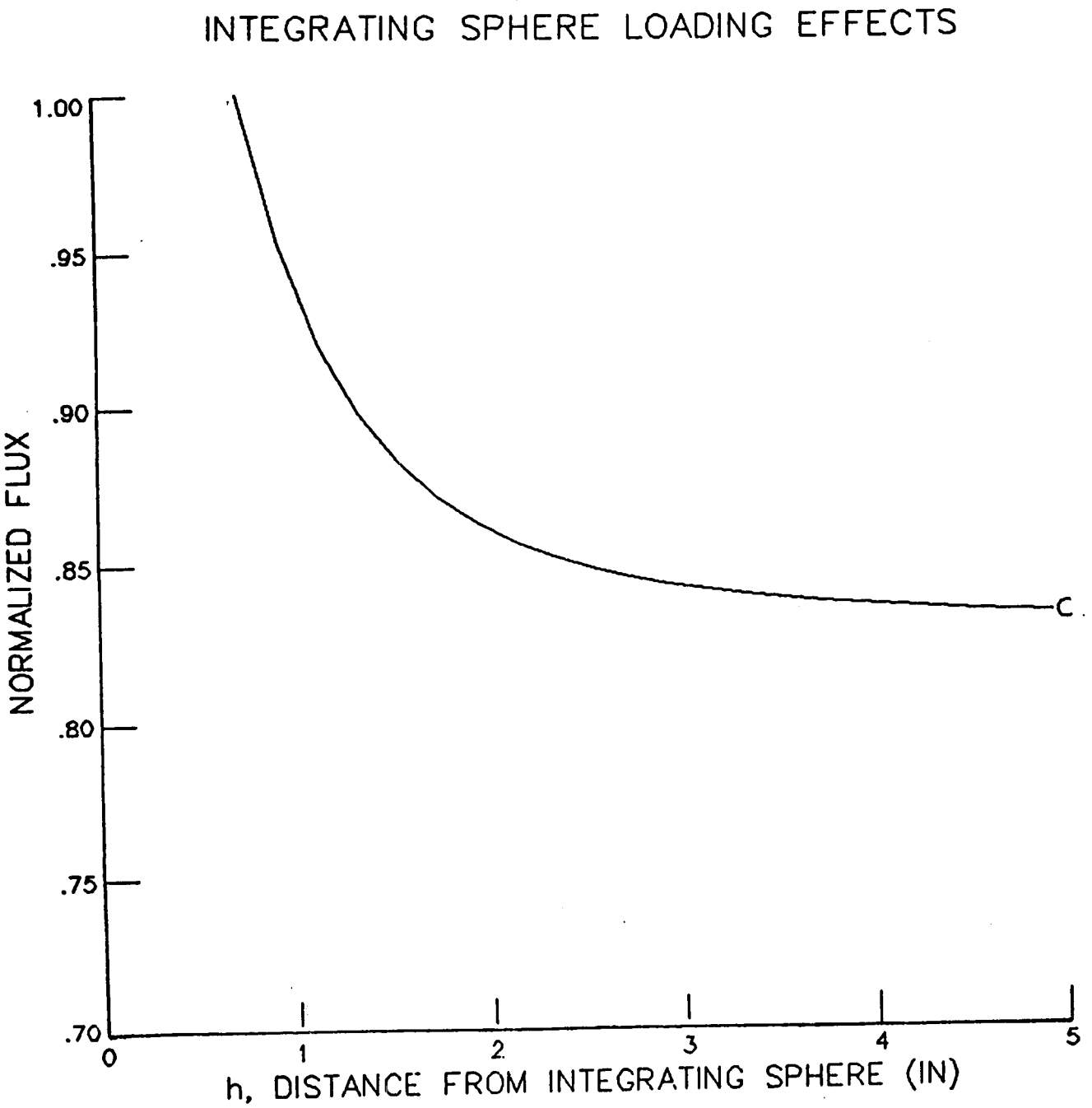

FIGURE 5(B). SHORTWAVE LOADING EFFECTS FOR THE MFOV TOTAL INSTRUMENT ($h_o = .744°$)

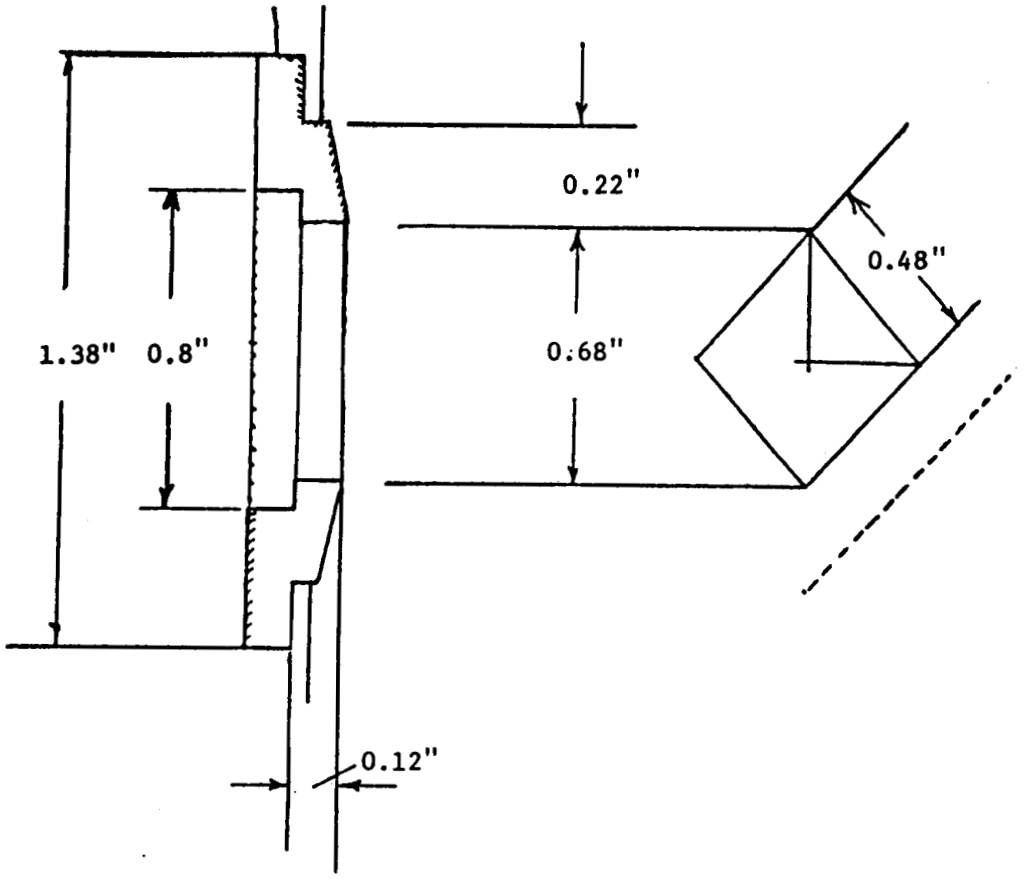

FIGURE 6. OPAL GLASS AND INSULATOR GEOMETRY

TABLE 1. WFOV TOTAL INSTRUMENT VERSUS PHOTO-DIODE CALIBRATION

$\Delta V(V)$	$\Delta E(W/m^2)$	$g\Delta V + \Delta E_\ell$	$\Delta E - (g\Delta V + \Delta E_\ell)(W/m^2)$
8.34801	274.18	273.78	-0.40
8.40880	275.30	275.75	0.45
8.44519*	275.39	276.94	1.54
7.06226	231.92	231.96	0.05
7.09124*	231.60	232.91	1.31
5.37728	177.73	177.17	-0.56
5.39272	178.30	177.67	-0.63
5.37571	177.37	177.12	-0.24
3.21880	107.14	106.98	-0.16
3.22939	107.59	107.32	-0.27

$$g = 32.52, \quad \Delta E_\ell = 2.3$$

$$\left[\sum_k \left|\Delta E_k - (g\Delta V_k + \Delta E_\ell)\right|^2\right]^{\frac{1}{2}} = .73 \ W/m^2$$

TABLE 2. MFOV TOTAL INSTRUMENT VERSUS PHOTO-DIODE CALIBRATION

$\Delta m^{P/M}$ (V)	Δm^{M} (W/m^2)	$g^{M}\,\Delta m^{P/M} + \Delta E_{\ell}^{M}$ (W/m^2)	Δn_1 = (error) (W/m^2)
8.33651	290.89	289.24	-1.64
8.34718	290.46	289.61	-0.85
8.34573	287.97	289.56	1.59
8.36678	288.85	290.28	1.44
7.25552	249.93	252.03	2.10
7.28618	252.23	253.09	0.86
5.23328	184.67	182.43	-2.24
5.26209	185.75	183.42	-2.33
5.27257	184.55	183.78	-0.76
5.27142	184.66	183.74	-0.91
3.11803	109.11	109.62	0.51
3.13004	108.46	110.04	1.58

$$g^{M} = 34.42,\ \Delta E_{\ell}^{M} = 2.3$$

$$\left[\sum_{k}\left|\Delta n_{1k}\right|^{2}\right]^{1/2} = 1.52$$

Standard Bibliographic Page

1. Report No.	2. Government Accession No.	3. Recipient's Catalog No.
NASA CR-178293		

4. Title and Subtitle	5. Report Date
Development of Response Models for the Earth Radiation Budget Experiment (ERBE) Sensors: Part II - Analysis of the ERBE Integrating Sphere Ground Calibration	March 20, 1987
	6. Performing Organization Code
7. Author(s)	8. Performing Organization Report No.
Nesim Halyo, Deborah B. Taylor	FR 687104
9. Performing Organization Name and Address	10. Work Unit No.
Information & Control Systems, Incorporated 28 Research Drive Hampton, VA 23666	665-45-30-01
	11. Contract or Grant No.
	NAS1-16130
12. Sponsoring Agency Name and Address	13. Type of Report and Period Covered
National Aeronautics and Space Administration Langley Research Center Hampton, VA 23665	Contractor Report
	14. Sponsoring Agency Code

15. Supplementary Notes

Langley Technical Monitor: Robert J. Keynton

Final Report

16. Abstract

An explicit solution of the spectral radiance leaving an arbitrary point on the wall of a spherical cavity with diffuse reflectivity is obtained. The solution is applicable to spheres with an arbitrary number of openings of any size and shape, an arbitrary number of light sources with possibly non-diffuse characteristics, a non-uniform sphere wall temperature distribution, non-uniform and non-diffuse sphere wall emissivity and non-uniform but diffuse sphere wall spectral reflectivity. A general measurement equation describing the output of a sensor with a given field-of-view, angular and spectral response measuring the sphere output is obtained. The results are applied to the Earth Radiation Budget Experiment (ERBE) integrating sphere. The sphere wall radiance uniformity, loading effects and non-uniform wall temperature effects are investigated. It is shown that using appropriate interpretation and processing, a high-accuracy shortwave calibration of the ERBE sensors can be achieved.

17. Key Words (Suggested by Authors(s))	18. Distribution Statement
Spectral Radiance, Spherical Cavity, Diffuse Reflectivity, Integrating Sphere, Loading Effects, Shortwave Calibrations	Unclassified - Unlimited Subject Category 35

19. Security Classif.(of this report)	20. Security Classif.(of this page)	21. No. of Pages	22. Price
Unclassified	Unclassified	50	A03

For sale by the National Technical Information Service, Springfield, Virginia 22161